

# Turbulent filament properties in L and H-mode regime in the RFX-mod operating as a tokamak

G. Grenfell<sup>1,2,3,\*</sup>, M. Spolaore<sup>1</sup>, D. Abate<sup>1</sup>, L. Carraro<sup>1</sup>,  
L. Marrelli<sup>1</sup>, I. Predebon<sup>1</sup>, S. Spagnolo<sup>1</sup>, M. Veranda<sup>1</sup>,  
M. Agostini<sup>1</sup>, B.Ph. van Milligen<sup>2</sup>, R. Cavazzana<sup>1</sup>, L. Cordaro<sup>1</sup>,  
G. De Masi<sup>1</sup>, P. Franz<sup>1</sup>, C. Hidalgo<sup>2</sup>, E. Martines<sup>1</sup>, B. Momo<sup>1</sup>,  
M. E. Puiatti<sup>1</sup>, P. Scarin<sup>1</sup>, N. Vianello<sup>1</sup>, B. Zaniol<sup>1</sup>, M. Zuin<sup>1</sup>  
and the RFX-mod Team

<sup>1</sup> Consorzio RFX (CNR, ENEA, INFN, Università di Padova, Acciaierie Venete SpA), C.so Stati Uniti 4, 35127, Padova, Italy

<sup>2</sup> National Fusion Laboratory, CIEMAT, Avda. Complutense 40, 28040 Madrid, Spain

<sup>3</sup> Current address: Max-Planck-Institut für Plasmaphysik, Boltzmannstr. 2, Garching, Germany

\* Corresponding author: gustavo.grenfell@ipp.mpg.de

## Abstract.

The dynamics of turbulent filaments in L and ELM-free H-mode in the RFX-mod device operating as a tokamak is discussed in the present work. L-H transition and sustained H-mode have been achieved in the RFX-mod with the aid of an external electrode biasing (M. Spolaore et al. 2017 Nucl. Fusion 57 116039). Through advanced statistical techniques, turbulent filaments are detected and tracked from the edge to the Scrape-Off Layer (SOL) in a two-dimension floating potential map (measured with a 2D array of Langmuir probes) related with extreme events of a fixed ion saturation current signal in the SOL. While in L-mode filaments travel almost freely, their motion becomes restricted to the near SOL during the induced biasing H-mode. In this region, the background shear decorrelation time becomes shorter than the convective filament time, favouring its suppression. However, the experimental observation of a nearly 'trapped' monopole potential points out the possible role of the vortex selection mechanism. The sign and magnitude of the turbulent parallel vorticity are consistent with the  $E \times B$  background vorticity in the SOL in this regime, while in L-mode, the inferred turbulent vorticity is always above the background one. The sparse filamentary transport in the far SOL during H-mode is further confirmed from the measurements of a poloidally symmetric array of electrostatic sensors on the wall. Lastly, the radial velocity of filaments in both regimes was discussed in the framework of analytical scalings. Filaments in L-mode exhibit a reasonable agreement with the sheath-limited regime in the cold ion approximation, with a non-negligible associated parallel current density measured with a set of 3-axial pickup coils installed in the probe head. In H-mode, the collisionality increases near the separatrix while filaments seem to follow the inertial regime before becoming trapped.

## 1. Introduction

The energy and particle transport in the Scrape-Off-Layer (SOL) of fusion devices is, at large extend, controlled by turbulent filaments or blobs [1, 2, 3, 4, 5]: structures denser than the surrounding plasma and aligned to the equilibrium magnetic field [6, 7]. Their motion is predominantly radially outward [8, 7] and boosted by an  $E \times B$  drift that follows the blob polarization induced typically by  $\nabla B$  and magnetic curvature drifts. A parallel current arises as a response to the charge building up to guarantee the plasma quasi-neutrality. The current closure path that is ultimately related to the collision frequency along the open field lines and the magnetic field topology strongly affects the filament dynamics [9, 10, 11] and, therefore, the penetration of blobs in the SOL. The propagation of filament from the edge to the SOL couples the turbulence of these two regions, enhancing the SOL fluctuation [12] and so the plasma-wall interaction.

Implications of filamentary transport have drawn more attention recently due to the issue of power exhaust in ITER [13], and the level of plasma-wall interaction in the main chamber, that must be kept as lower as possible to avoid damage of the plasma-facing components and the influx of impurity to the confinement region [14]. The SOL density and temperature profiles are the results of the competition between parallel (toward the divertor) and cross-field transport in first approximation [15]. While the former is governed by classical transport, the latter is dominated by turbulence [16, 17], with turbulent filaments playing a pivotal role [18, 19]. In addition, turbulent simulations have suggested that the cross-field transport in the plasma edge and SOL of ITER will be dominated by blobs [17, 20], which has a beneficial effect for energy exhaustion since the heat would be spread over a broader area. Therefore, the proper understanding of the blobs dynamics in different plasma conditions and backgrounds have become a requirement for future machines.

On the other hand, sheared flows is a critical parameter to regulate turbulent cross-field transport in fusion devices [21, 22, 12, 23]. The plasma background can modify the dynamics of filaments, besides of being modified by them [8, 24, 25]. Filaments with a specific size and cross-field velocity can be torn apart or trapped by large enough shear flows [26, 27, 28, 29, 25]. Edge  $E \times B$  shear flow, either mean or oscillating, is commonly thought to be responsible for the L-H transition in both tokamaks and stellarators [30, 21]. However, the mechanism that generates this flow is not entirely understood [31, 32, 33]. Filaments appear as a candidate for that, possibly through Reynolds stress mechanism [16, 34]. The observed blob tilt related to  $E \times B$  flow and magnetic shear [35, 3] seem to agree with this idea [36]. Experimentally, the edge profile of the radial electric field ( $E_r$ ) can be modified with the aid of an external electrode biasing in colder plasmas [37]. Such a technique has been shown to induce L-H transition in both tokamak [38, 39], and stellarator [40], by enhancing  $E_r \times B$  flows in the plasma boundary. In the RFX-mod operating as a tokamak, H-mode has been achieved with an external biasing placed at its edge in both circular and single-null plasmas, where, in some cases, Edge-localized mode (ELM) like structures were observed [41].

In this paper, we present experimental results on turbulent filament features employing a two-dimension array of electrostatic and magnetic probes. The aim is to study their dynamics in two plasma regimes in the RFX-mod operating as tokamak: regular ohmic L-mode and biasing ELM-free H-mode. In section 2, the experimental setup of the RFX-mod running as a tokamak is described. Section 3 presents the experimental results, highlighting the role of  $E \times B$  background flows in suppressing turbulence in the plasma edge and their impact on the filament dynamics in L and H-mode, and consequences for the level of plasma-wall interaction in the main chamber. Besides, through the measurements of the parallel current density, parallel transport is discussed in the framework of analytical models. We present our conclusions in section 4.

## 2. Experimental setup

RFX-mod is a toroidal device, with minor radius  $a = 0.46$  m and major radius  $R_0 = 2$  m. The machine was designed to operate as a reversed field pinch (RFP) with plasma current up to 2 MA [42]. The MHD control system of RFX-mod [43] supports this requirement by inhibiting the growth of instabilities that otherwise would lead to the fast plasma ending. Such a system is equipped with 192 saddle coils that cover the entire torus [42, 44]. Besides, owing to its flexibility, RFX-mod can also operate as a low current tokamak [41]. The plasma shape, in this case, is feedback-controlled, allowing operation in both circular or single null configuration; in the latter with X-point either at the top or bottom. Typical plasma duration in tokamak configuration is about 1 s, with plasma current  $I_p \leq 150$  kA, and toroidal magnetic field  $B_\phi \leq 0.55$  T. In addition, specific experiments based on electrode biasing were performed, where a stable and reproducible H-mode regime was observed [41].

The following results are from RFX-mod operating as ohmic single null tokamak [41], with the  $\nabla B$  drift towards the X-point. The plasma current in all considered shots was  $I_p \leq 50$  kA, the central line averaged density varied within the range:  $(2 - 6) \times 10^{18}$  m<sup>3</sup>, and the magnetic field on axis was up to 0.55 T (counter-clockwise when viewed from the top). In this configuration, the edge safety factor is in the range  $q_{95} = (3 - 4)$ . In addition, the plasma was externally modified with a graphite electrode ellipsoid shaped (115 mm $\times$ 25 mm $\times$ 65 mm) placed at the bottom of the vacuum vessel and biased with respect to the wall (Fig. 1 a). The delivered voltage was  $U_b \approx -400$  V in a squared 400 ms voltage pulse (Fig. 2 b). The electrode was placed and kept 8 cm inside the last closed flux surface (LCFS) or at  $r/a \approx 0.83$ . Such configuration was shown to induce H-mode in the RFX-mod tokamak in both circular and single null-configuration [41].

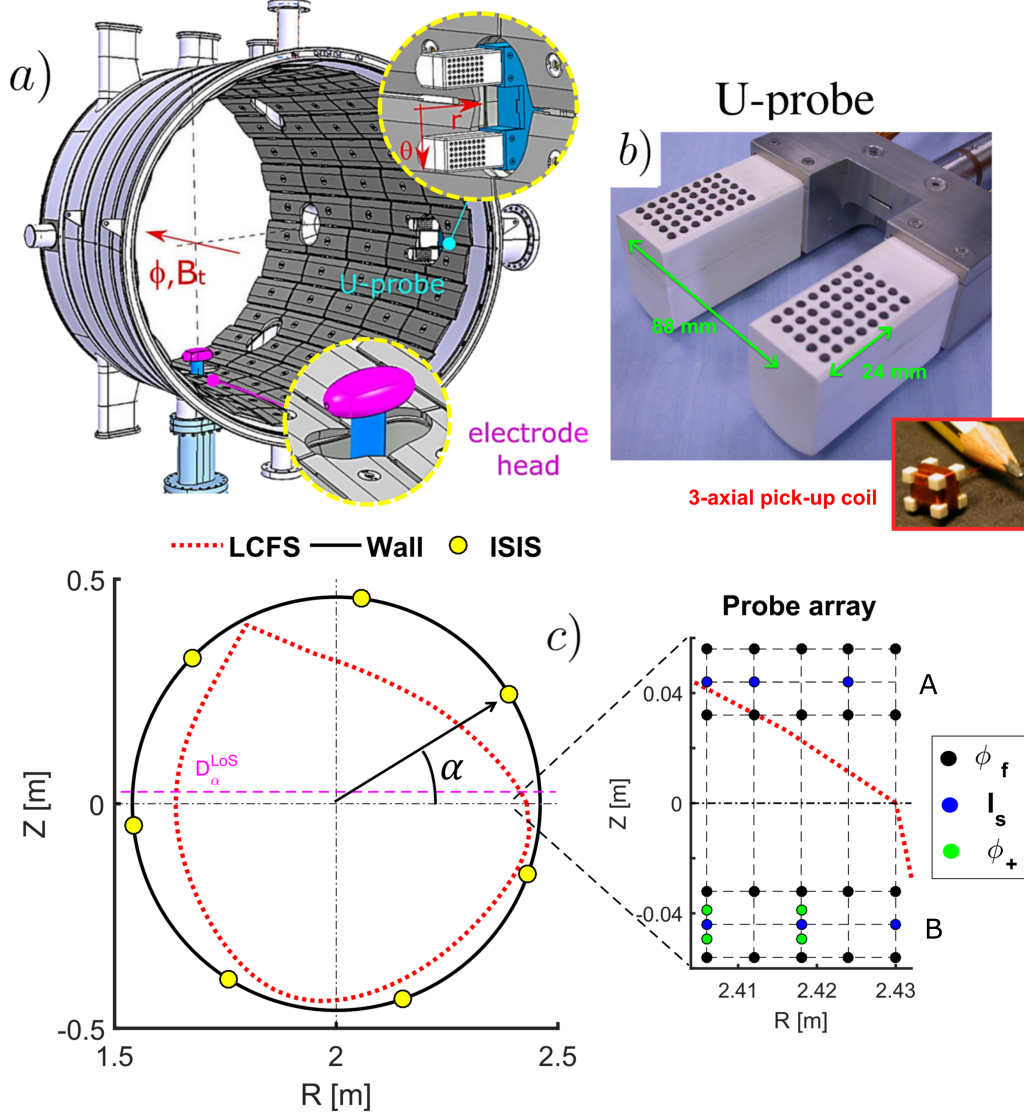
The plasma edge and SOL are monitored with an insertable Langmuir probe (hereinafter referred to U-probe ) composed of two towers spaced 88 mm (roughly in the bi-normal or poloidal direction), Fig. 1 b). The probe has 40 graphite tips (5x8 array) installed in each tower, with 5 tips per row aligned poloidally and spaced 6 mm

from each other, and 8 tips in each column aligned radially and spaced 6 mm (Fig. 1 b and c). In addition, each tower is also equipped with seven 3-axial pick-up coils measuring simultaneously the time derivative of three components of the local magnetic field,  $\dot{B}_r$ ,  $\dot{B}_\theta$ , and  $\dot{B}_\phi$ . The coils are installed inside the probe body placed at the center of each tower, with mutual radial separation of  $\sim 6$  mm. The boron nitride (BN) cover is virtually transparent to measured magnetic fluctuations. In this experiment, only the five innermost coils in each tower were connected. The probe was inserted from the outboard midplane (Fig. 1 c), displaced approximately  $15^\circ$  toroidally from the bias electrode. The working configuration was the following: 3 radially spaced ion saturation current ( $I_s \propto n_e T_e^{1/2}$ , where  $n_e$  and  $T_e$  are, respectively, the electron density and temperature) and 10 floating potential ( $\phi_f$ ) signals, in a 2x5 array, in each tower, covering a total 2D cross-field range of  $\sim 112 \times 24$  mm (Fig. 1 c). Besides, the electron temperature ( $T_e$ ) was measured in two positions in the plasma edge with the modified five-pins balance triple probe method [45], in which  $T_e = (\phi_+ - \phi_f)/\ln(3)$ , where  $\phi_+$  is a positive biasing configured in a double probe circuit such as  $\phi_+ - \phi_- \gg T_e/e$ , where  $\phi_-$  is the negative biasing to collect the ion saturation current. Data of all probe signals were acquired at 2 MHz sampling frequency rate.

To monitor fluctuations near the plasma wall, we considered data from the Integrated System of Internal Sensors (ISIS) composed of a set of electrostatic and magnetic sensors installed on the wall of RFX-mod, and covering the entire torus [46]. We focused, however, on the ISIS electrostatic poloidal array sensors (Fig. 1 c), yellow circles), set to measure floating potential. The whole system is  $\sim 30^\circ$  toroidally shifted from the U-probe, which allows us to inquire about the 3D nature of turbulent filaments (section 3.6). The LCFS is reconstructed in real-time ( $\sim 1$  ms) by extrapolating both poloidal magnetic flux and magnetic field measurements in the vacuum region [47]. Fig. 1 c) shows the LCFS reconstruction in L-mode.

### 3. Experimental results

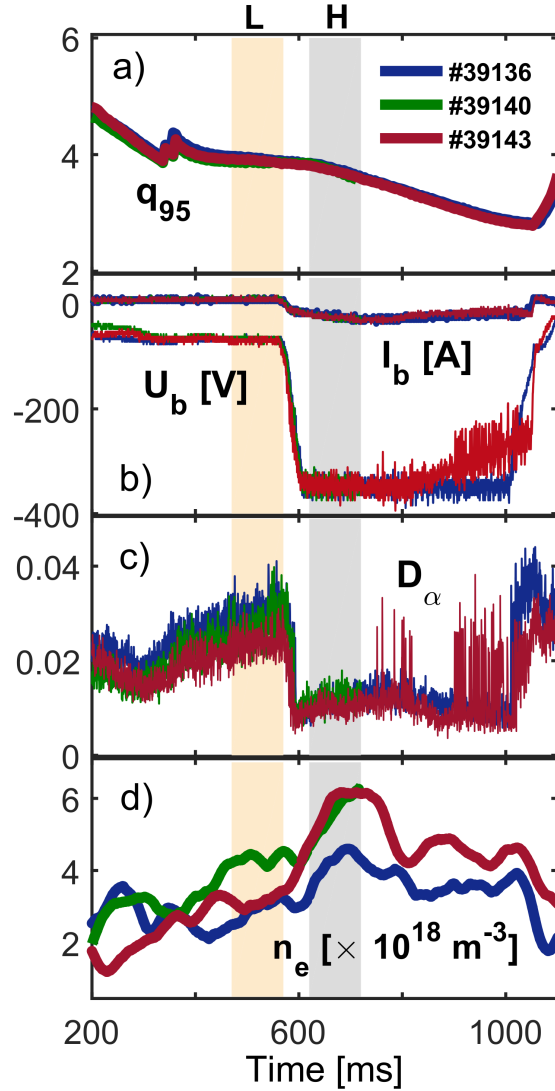
In this work, three reproducible shots were taken into account to study the dynamics of filaments in both L and ELM-free H-mode (Fig. 2). They all exhibit a similar behaviour over time: the  $D_\alpha$  line (Fig. 2 c) drops when biasing is applied, followed by an increase of the central line averaged density - compatible with the typical particle confinement improvement observed in edge biasing experiments [37, 1, 39]. The plasma current was  $I_p \leq 50$  kA, slightly ramped-up during biasing, which reflects in the decreasing of  $q_{95}$  (Fig. 2 a). Note that the  $D_\alpha$  line drops before the biasing voltage ( $U_b$ ) reaches its minimum, suggesting that there is a biasing voltage threshold preceding the L-H transition. The density is below  $0.6n_G$ , where  $n_G = I_p/(\pi a^2)$  is the Greenwald density and  $a \approx 0.4$  m, which is relatively safe for high triangularity of the poloidal cross-section [48]. In the shot #39140 (plotted in green), however, the density increases up to approximately  $0.6n_G$ , which is the possible reason for a disruption around 750 ms. Similar behavior is also seen in the #39143 (red), but the price to pay in this case seems



**Figure 1.** a) schematic picture showing a poloidal section of RFX-mod with the U-probe inserted at the midplane low field side and the biasing electrode from the bottom part. b) picture of U-probe showing the two towers displaced 88 mm (from their center, approximately in the binormal direction) and the two arrays of pins. The red rectangle shows a picture of one of the 3-axial pick-up coils that are installed inside the two towers (7 each). c) shows the last closed flux surface (LCFS) reconstruction [47] and the ISIS poloidally symmetric array of Langmuir probes installed on the wall. Here  $\alpha$  represents the poloidal position of the ISIS sensors (counterclockwise with respect to the midplane) shown in Fig. 20. The magenta dashed line corresponds to the light of sight of the  $D_\alpha$  line shown in Fig. 2 c). The position of the 2D array of probes and the working configuration, where the colors refer to floating potential ( $\phi_f$  - black), ion saturation current ( $I_s$  - blue), and positive potential ( $\phi_+$  - green). The two towers are labelled as A and B.

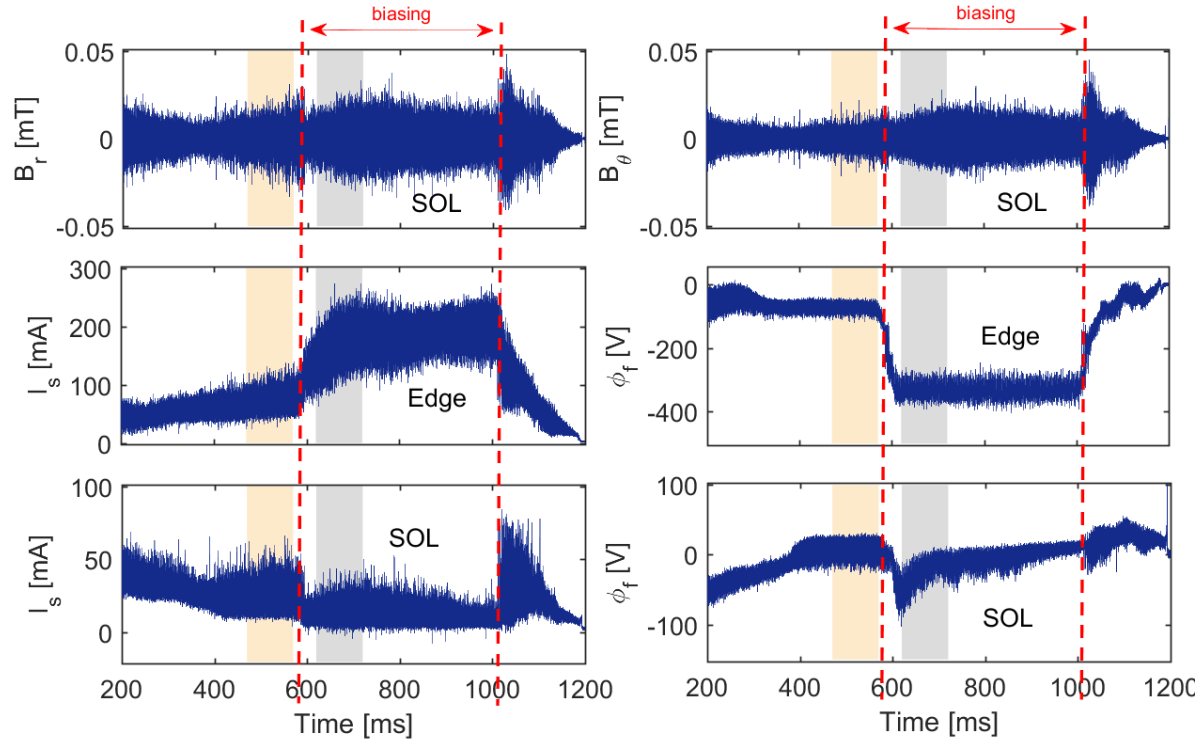
to be the rise of an ELM-like instability.

Fig. 3 shows typical signals measured with the U-probe. At the top panel, it is



**Figure 2.** L-H transition in RFX-mod running as tokamak induced by an external electrode biased inserted 8 cm into the plasma edge ( $r/a \approx 0.83$ ). a) edge safety factor, b) biasing voltage and drained current, c)  $D_\alpha$  line at the midplane, and d) central line averaged density for three shots: #39136, #39140 and #39143. The two colourful regions behind each graph represent the time windows considered in the turbulent filament analysis.

shown the radial and poloidal components of the magnetic field fluctuation in the SOL ( $r - r_0 \approx 0.8$  cm, where  $r_0$  is the LCFS position that minimizes  $r$ ). They were obtained by time integrating the coil signal corresponding to the magnetic field component, considering the contribution of its effective area. The magnetic fluctuations slightly decrease right after the biasing is applied but increase later, keeping roughly the same level as before (L-mode). The effect of biasing on the ion saturation current ( $I_s$ ) and floating potential ( $\phi_f$ ) in the edge ( $r - r_0 < 0$ ) and SOL ( $r - r_0 > 0$ ) is shown in the middle and bottom panels. While in the edge,  $I_s$  increases and  $\phi_f$  becomes further negative,



**Figure 3.** Time trace of some of the U-probe signals during the biasing L-H transition in RFX-mod running as tokamak (#39136).

in the SOL, both  $I_s$  and  $\phi_f$  slightly decrease. The significant difference between the floating potential in the edge and SOL results in a steeper  $\phi_f$  radial profile, as it is shown in section 3.1.

### 3.1. $E \times B$ background flow

Sheared  $E \times B$  background flows is the key parameter that leads to the L-H transition [30, 49], by stabilizing turbulence [26] that, otherwise, would result in large cross-field fluxes. Fig. 4 a) shows the mean floating potential represented in a two-dimension map measured with the U-probe in L and H-mode. The dashed black line represents the LCFS position. The map was computed over a time window before (470-570 ms) and during (620-720 ms) biasing. Two-dimension quadratic interpolation was applied to better visualize the image. One can note that the equipotential curves roughly follow the curvature of the magnetic field. Fig. 4 b) shows the radial profiles of the floating potential in L and H-mode, where the x-axis shows the shortest radial distance from the measured point to the LCFS. A third-order Savitsky-Golay filter [50] was applied in each case to smooth the interpolated curves (full lines). It is possible to notice the strong modification of  $\phi_f$  during biasing, with the edge potential reaching values comparable to the biasing voltage, resulting in a steeper profile. The  $E \times B$  poloidal rotation is obtained from the radial derivative of the  $\phi_f$  fitted curves,  $v_\theta^{E \times B} = E_r/B \sim -\nabla_r \phi_f/B$  (Fig. 4 c). The error bars correspond to the uncertainties

from the derivative and the ensemble error since the derivative was performed every 2 ms. In H-mode, an enhanced  $E \times B$  shear layer flow is established around the LCFS, with  $|v_\theta^{E \times B}|$  increasing up to approximately  $-20$  km/s. The  $E \times B$  shearing rate (Fig. 4 d) was obtained from the derivative of  $v_\theta^{E \times B}$ ,  $\gamma_{E \times B} \sim dv_\theta^{E \times B}/dr$ . The error bars again correspond to the uncertainties on the derivative and the ensemble error. The shear layer established in H-mode yields a positive and negative shear zone with values up to  $|\gamma_{E \times B}| \approx 1 \times 10^6 \text{ s}^{-1}$ .

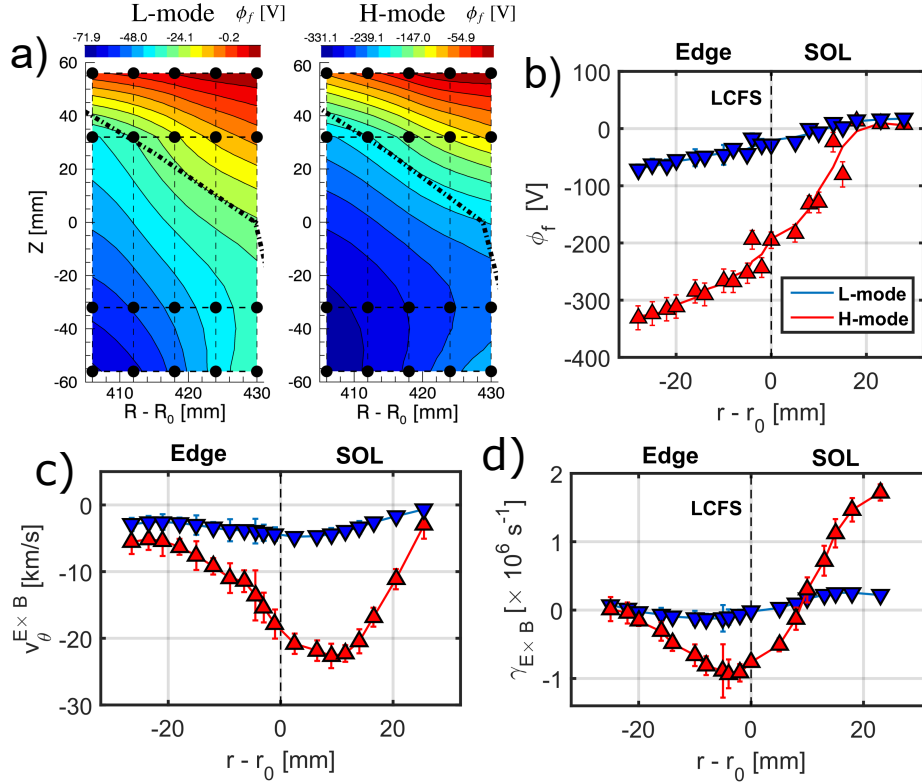


**Figure 4.** a) two-dimension floating potential map measured with the U-probe in L-mode and H-mode, the dot points in black show the grid covered by the  $\phi_f$  2D array. Radial profiles of b) floating potential, c)  $E \times B$  flow projected in the poloidal direction ( $v_\theta^{E \times B} \sim -\nabla_r \phi_f / B$ ), and d)  $E \times B$  shearing rate ( $\gamma_{E \times B} \sim dv_\theta^{E \times B} / dr$ ) in L and H-mode, blue and red, respectively. The black dashed line represents the LCFS position, while  $r = \sqrt{(R - R^*)^2 + (Z - Z^*)^2}$ , where  $(R^*, Z^*)$  is the separatrix position that minimizes  $r$ , i.e., that gives the shortest distance between the probe and the LCFS boundary (#39136).

Fig. 5 a) shows that the ion saturation current profile becomes steeper during biasing, while its SOL baseline decreases. On the other hand, the electron temperature in the near edge does not change much (Fig. 5 b) in the same radial interval. It is worth noting that the ion saturation current profile is closely connected to electron density one ( $I_s \propto n_e T_e^{1/2}$ ) since the electron temperature does not vary much. The steepness  $I_s$  (or  $n_e$ ) radial profile with lower SOL baseline values are signatures of the rise of an edge transport barrier in this region. In addition, the weak modification of  $T_e$  compared to

$\phi_f$  suggests that the radial electric field ( $E_r = -\nabla_r \phi_p$ , where  $\phi_p \simeq \phi_f + 3T_e$ ) is mostly set by the floating potential variation.

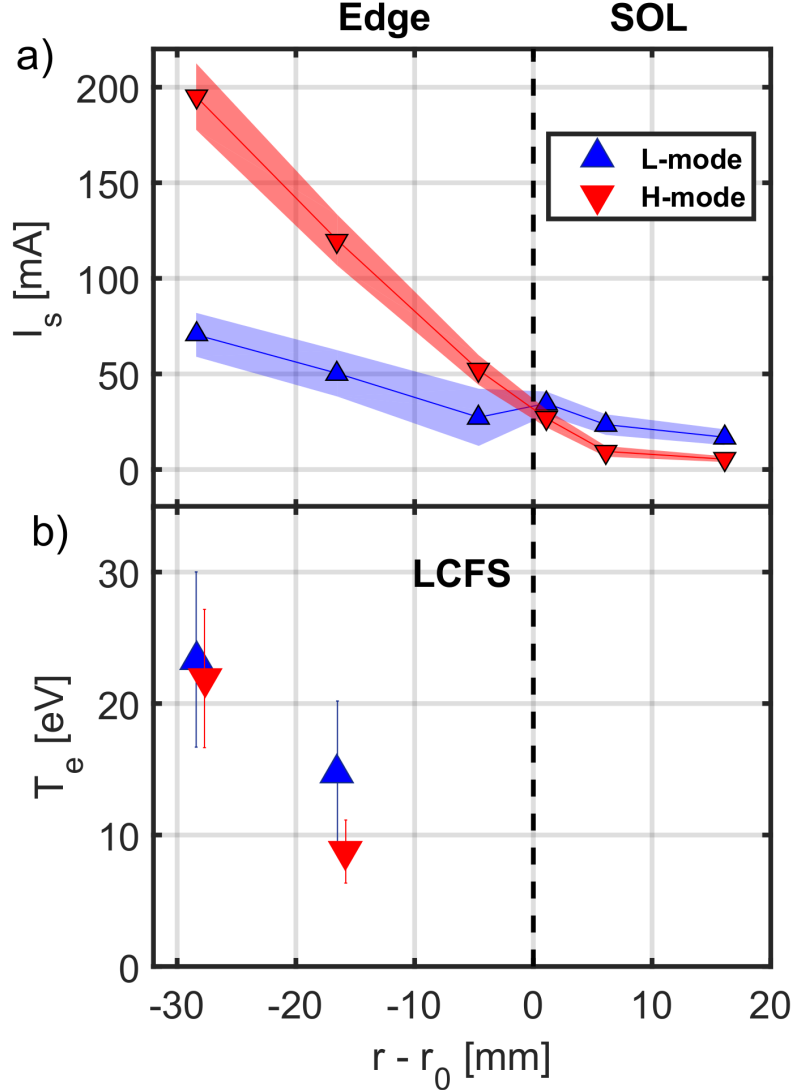


**Figure 5.** a) ion saturation current and b) electron temperature profiles in L and H-mode. The black dashed line represents the LCFS position (#39136).

Enhanced sheared radial electric fields was recently shown to be capable not only to suppress turbulence locally but also to block its propagation from the edge into the SOL in the TJ-II stellarator [12]. This phenomenon ultimately affects SOL profiles [17], since cross-field turbulent transport is reduced [12]. To verify the level of SOL turbulence penetration in RFX-mod, the radial cross-correlation technique was applied in 5 pins at the same column of U-probe (Fig. 1, tower A upper column), all located in the SOL region and configured to measure floating potential. The turbulent correlation length is usually considered as the range where the correlation is higher than a threshold around a reference (auto-correlation) at zero delays, e.g., higher than  $1/e$  for exponential decay.

We decided, however, to consider the maximum correlation at any time delay in order to account for turbulence propagation. Since filamentary transport is believed to be responsible for establishing the SOL, together with parallel transport, this approach seems to be more appropriate to characterize the SOL turbulence. The  $\phi_f$  signals were high pass filtered ( $> 15$  kHz) to eliminate the influence of low-frequency modes. The correlation was calculated in 4 ms time slices, and the result is shown in Fig. 6. The chosen reference is placed near the LCFS ( $r - r_0 \approx 6$  mm). One can see intermittent events penetrating the SOL before biasing (L-mode), keeping high correlation with the reference signal. During biasing, however, a very high correlation is found near the reference, but it sharply drops further out, hence, reducing the higher correlation range. The effective radial correlation length ( $L_r^*$ ) is calculated by fitting an exponential function starting from the reference floating potential, i.e., the e-folding length of the maximum cross-correlation  $L_r^* = [-\nabla_r \log \mathbf{Max}(Corr)]^{-1}$ . The bottom panel of Fig. 6 shows that the correlation length drops from around 20 mm to 8 mm when biasing is on. This result supports the idea of a transport barrier that prevents the propagation of high correlated structures from the edge into the far SOL. In addition, the bottom panel of Fig. 6 also shows the e-folding length of the mean ion saturation current profile (Fig. 5) over time, i.e.,  $\lambda_{I_s} = [-\nabla_r \log \langle I_s \rangle]^{-1}$ , where we note that the profile is well fitted by a single exponential function. The drop of  $\lambda_{I_s}$  (which is closely related to the density decay length around the LCFS,  $\lambda_n$ ) indicates that the profile becomes steeper during biasing (H-mode), and it follows the trend of  $L_r^*$ , in qualitative agreement with the mixing length hypothesis  $\tilde{n}/\langle n \rangle \sim L_r^*/\lambda_n$ , since  $\tilde{n}/\langle n \rangle \sim \tilde{I}_s/\langle I_s \rangle \sim 0.2$  around the LCFS before and during biasing. The disagreement in the absolute value is partially due to the definition of the mixing length here, i.e., from the maximum of the correlation instead of at zero delay that naturally gives larger values [23]. Nevertheless, this result shows that the relaxation of the  $I_s$  profile is related to wider penetration of turbulence in the SOL, leading to a larger mixing length.

### 3.2. Filament dynamics in L and H-mode

Filaments typically appear in the SOL region of fusion devices with density higher than the surrounding background plasma and a non-Gaussian Probability Distribution Function (PDF) [7]. In previous studies, turbulence simulations of RFX-mod SOL running as tokamak for circular ohmic discharges were confronted with experimental observations of  $I_s$  and  $\phi_f$  fluctuations, indicating that the inertial drift wave instability accounts for most of the cross-field transport in this region [51]. However, further investigation is required to uncover the driven instability in the present experiment, which is beyond the scope of this paper. Fig. 7 a) compares the PDF of an ion saturation current signal in the SOL in L and H-mode. In both cases, a skewed PDF is evident, depicting the intermittent nature of the  $I_s$  fluctuations in this region.

Filaments or blobs are identified here from the extreme events of a reference ion saturation current signal. They are defined as the events higher than  $2.5\sigma$  (Fig. 7 a)

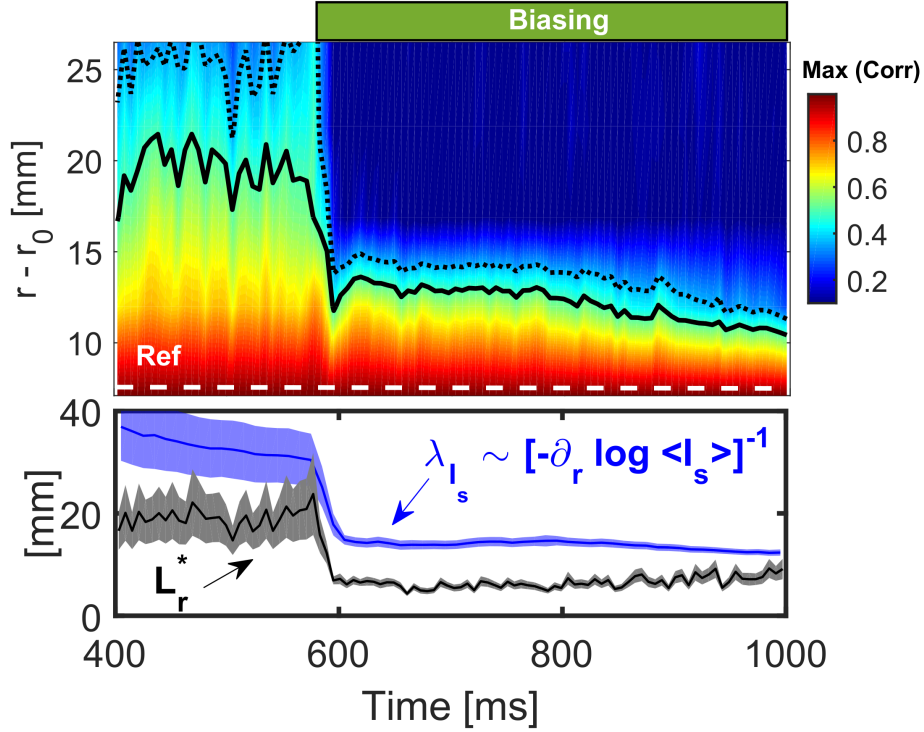


**Figure 6.** Top: maximum correlation (reference pin in the SOL,  $r - r_0 \approx 6$  mm). The full and dotted black lines represent, respectively, the correlation at 0.5 and  $1/e$  levels. The bottom figure shows the correlation length computed from an exponential fit starting from the reference position. In addition, the mean ion saturation current e-folding length ( $\lambda_{I_s}$ ) from the profile shown in Fig. 2 a) is shown in blue (#39136).

with respect to the mean sampling ( $\langle I_s \rangle$ ), where  $\sigma$  is the standard deviation. Similar threshold has also been used in previous blob studies [53, 4]. The choice is due to the fact that most of the intermittent events appear with an amplitude higher than the chosen threshold. The fluctuations were taken in the range 2-800 kHz to eliminate signal trend and high-frequency oscillations. Through the conditional average technique [52], the  $I_s$  intermittent events selected with the threshold criterion are averaged over a time slice around each peak, in a time window much longer than the time that the blobs remained in the frame covered by the probes. The reference tip is located at the near SOL ( $r - r_0 \approx 6$  mm). The conditional average is then extended to all the tips measuring  $I_s$  and  $\phi_f$  to capture the Spatio-temporal filament behaviour. Fig. 7 c) shows the conditional average of three ion saturation current signals ( $\delta I_s$ ) in the SOL during L-mode, where the reference is represented in red. One can see three peaks shifted in time, suggesting that the blob is propagating radially. Fig. 7 d) shows the conditional average of the same three ion saturation current signals, with the same reference and criterion but in H-mode. Note that in this case, the peaks are lower and narrower in time. This simple example shows how different blobs are in these two regimes.

Fig. 7 c) suggests that blobs propagate radially towards the wall, deduced from

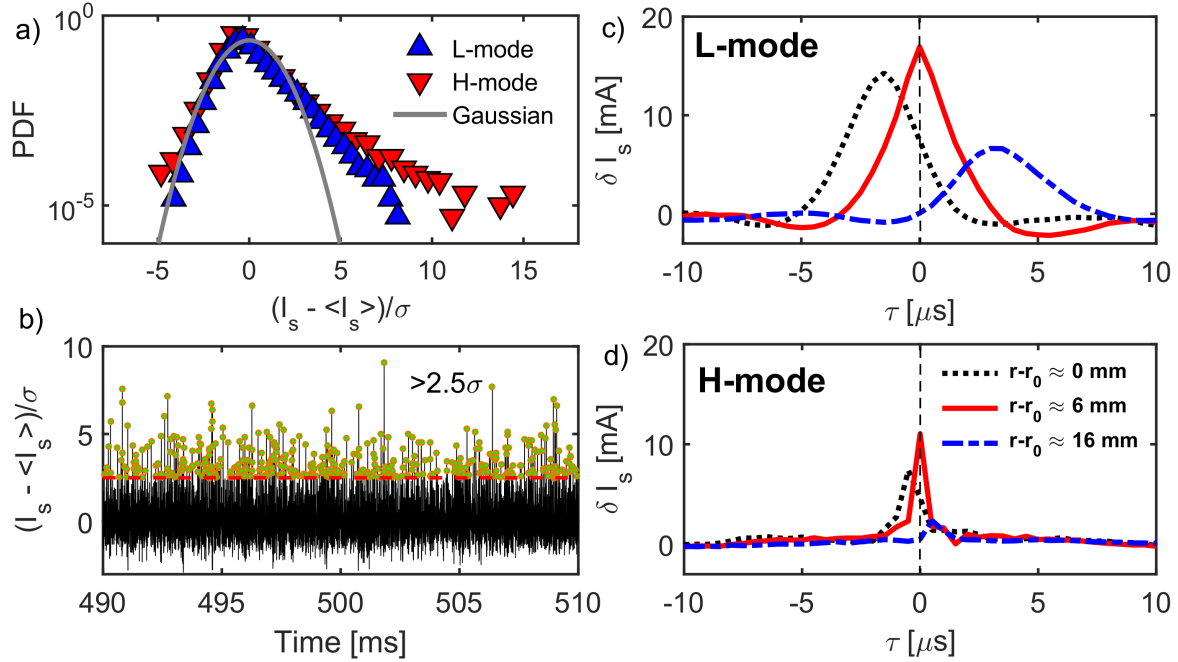


**Figure 7.** Ion saturation current blob: a) probability distribution function (PDF) in L and H-mode, b) normalized ion saturation current signal over time during L-mode, where the dashed line represents the threshold amplitude and the yellow circles the detected local maxima. Conditional ion saturation current ( $\delta I_s$ ) in c) L-mode and d) H-mode (#39136).

the time delay and radial displacement between pins. However, if the blob dimension is larger than the distance between pins, the projection of its poloidal rotation over the radial direction could yield a similar effect as long as the blob is tilted. Therefore, to disentangle that, one has to use at least three independent probes arranged in a non-collinear way in the cross-field plane [53]. The two-dimension floating potential array is employed for this purpose.

Fig. 8 shows the two-dimension conditional averaged floating potential ( $\delta\phi_f$ ) map in sixteen-time frames during L-mode, where  $\tau = 0$  corresponds to the time instant when the  $I_s$  reference (Fig. 7 c) peaked. To better visualize the image, the conditional floating potential array was quadratically interpolated at each frame. The black, red, and blue small circles shown in Fig. 8 indicate the position of the three  $I_s$  signals in Fig. 7 c). The white arrows represent the  $E \times B$  flow:  $\mathbf{v}^{E \times B} \approx -\nabla\phi_f \times \mathbf{B}/B^2$ , neglecting temperature fluctuation. Fig. 8 depicts a potential dipole structure related to the  $I_s$  blob. Notably, at  $\tau = 0 \mu\text{s}$ , the amplitude of the reference  $I_s$  (red circle) is maximum, and the centre of the dipole (middle distance from the positive to the negative pole) roughly lies at the same position, in agreement with the classical view of a dipole potential structure propelling a density blob through  $E \times B$  drift [7]. The sequence of frames shows clearly the  $\phi_f$  structure propagating from the edge into the SOL with a trailing wake. In addition, the parallel vorticity ( $\omega_{\parallel} = \nabla_{\perp} \times \mathbf{v}^{E \times B}$ ) becomes clearer from the flow

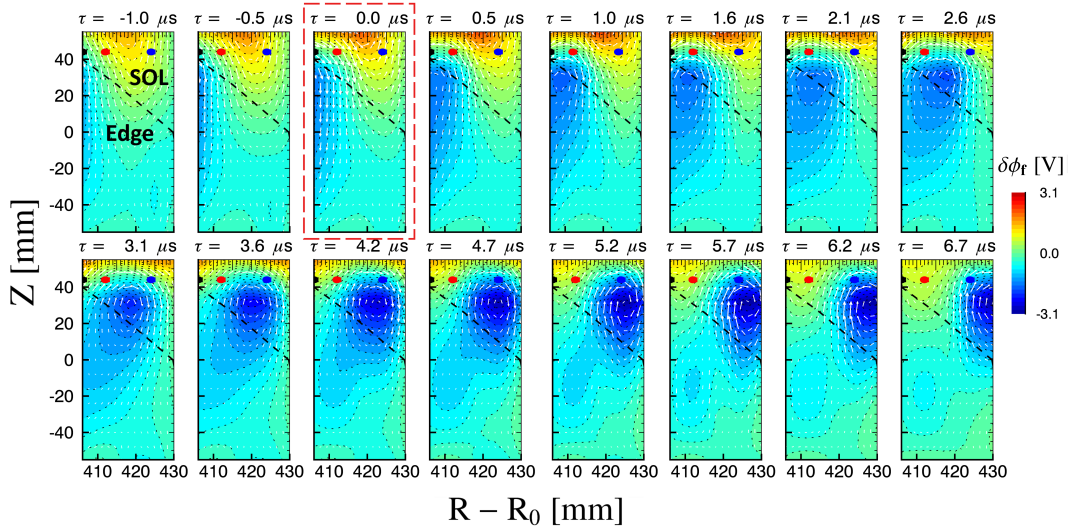


**Figure 8.** Conditional average of filaments detected with the threshold criterion as seen from a 2D floating potential map in sixteen frames during L-mode (#39136). The white arrows represent the  $E \times B$  flow. One can notice a dipolar structure emerging from the plasma edge and propagating towards the SOL, with an interchange character, as observed in the frame  $\tau = 0$ , where the  $I_s$  peak is out of phase with respect to the potential blob.

pattern around the negative potential as the filament moves into the SOL. Since the 2D region spanned by the U-probe does not allow to visualize the positive potential fully, we considered the negative pole as the reference for the investigation of the cross-field filament properties in the following. We note that each of the potential poles can be comparable to density/pressure blob as observed experimentally [55, 56]). Nevertheless, in H-mode, the background  $E \times B$  shear flow can affect the blob density and potential differently [29, 36].

As evidenced from Fig. 8, the potential filament structure is perceived to move towards the wall. A method based on the 2D cross-correlation was applied between subsequent frames to substantiate this qualitative observation into a more quantitative evaluation. The analysis is based on tracking the negative part of the floating potential structure. Fig. 9 shows an example of this technique applied to two subsequent frames during L-mode. The 2D cross-correlation (2D-CC) is computed by summing up all the terms yielding from the element-by-element products of the two superposed image or matrixes. The map is then obtained by shifting one image along with the R and Z-axis with respect to the other and calculating 2D-CC in each case, where the no overlap terms are set to zero. In Fig. 9 b), the yellow diamond symbol indicates the maximum of 2D-CC ( $0 \leq 2D-CC \leq 1$ ), thus giving the vertical and horizontal displacement of the potential structure. Since the time delay between the two frames is known, the 2D velocity is straightforwardly obtained. To assure that the blobs do not change much between subsequent frames, we imposed that the maximum 2D-CC must be larger than 0.8 (based on empirical observations). The blob size, however, was defined from the

2D autocorrelation (2D-AA) to avoid distortions caused by the blob velocity. In order to rule out boundary deformations, since blobs can be larger than the region spanned by the probe, we considered the blob extension as the 2D autocorrelation points larger than a suitable threshold that still allows resolving the blob shape. These points define a surface in the geometrical frame (R-Z). Alternatively, they can be visualized in a convenient plasma frame defined here as  $r = \sqrt{(R - R^*)^2 + (Z - Z^*)^2}$ , where  $(R^*, Z^*)$  is the separatrix position that minimizes  $r$  and  $\theta = \tan^{-1}[(Z - Z^*)/(R - R^*)]$ . Note that from this definition  $r_0 = \sqrt{(R^*)^2 + (Z^*)^2}$ . The dispersion extension of points in the plasma frame defines the radial and poloidal size of the blob. Those points are then approached by an ellipse through the eigendecomposition of the corresponding covariance matrix. This technique finds the direction in the space that gives the maximum covariance (principal axis), which might or not be tilted. The covariance matrix is defined as:

$$\Sigma = \begin{bmatrix} c_{xx} & c_{xy} \\ c_{yx} & c_{yy} \end{bmatrix} \quad (1)$$

where the sample covariance is  $c_{xy} = 1/(N-1) \sum_{k=1}^N (x_k - \bar{x})(y_k - \bar{y})$ , with  $N$  the number of points corresponding to the coordinates  $x_k$  and  $y_k$ , while  $\bar{x}(\bar{y}) = 1/N \sum_{k=1}^N x_k(y_k)$ . Through a linear transformation, one can write  $\Sigma$  as:

$$\Sigma V = V L \quad (2)$$

$V$  and  $L$  are, respectively, the eigenvectors and the eigenvalues matrices of  $\Sigma$ . Hence, the covariance matrix can be rewritten:

$$\Sigma = V L V^{-1} \quad (3)$$

where, from the single value decomposition (SVD) [57],  $V$  could be identified as a rotation matrix and  $\sqrt{L}$  as a scale matrix.

It follows from the previous equations that the eigenvector of the largest eigenvalue points out to the largest covariance, while the other vector is orthogonal to it. Therefore, the eigenvalues give the major and minor axes of an ellipse and the eigenvectors its orientation in the space. In Fig. 9 c) is shown an example of this technique applied to a potential structure in the edge. The chosen threshold of the 2D-AA for determining the blob extension was 0.8, which is robust enough to depict its shape without crossing the space resolution constrained by the probe pins, while it avoids including spurious fluctuations that might appear after conditional averaging the blob ensemble. The actual blob radial and poloidal size were then obtained by assuming a 2D Gaussian shape centred in the maximum correlation, where the size is given at Full Width at Half Maximum (FWHM) of the 2D autocorrelation, yielding

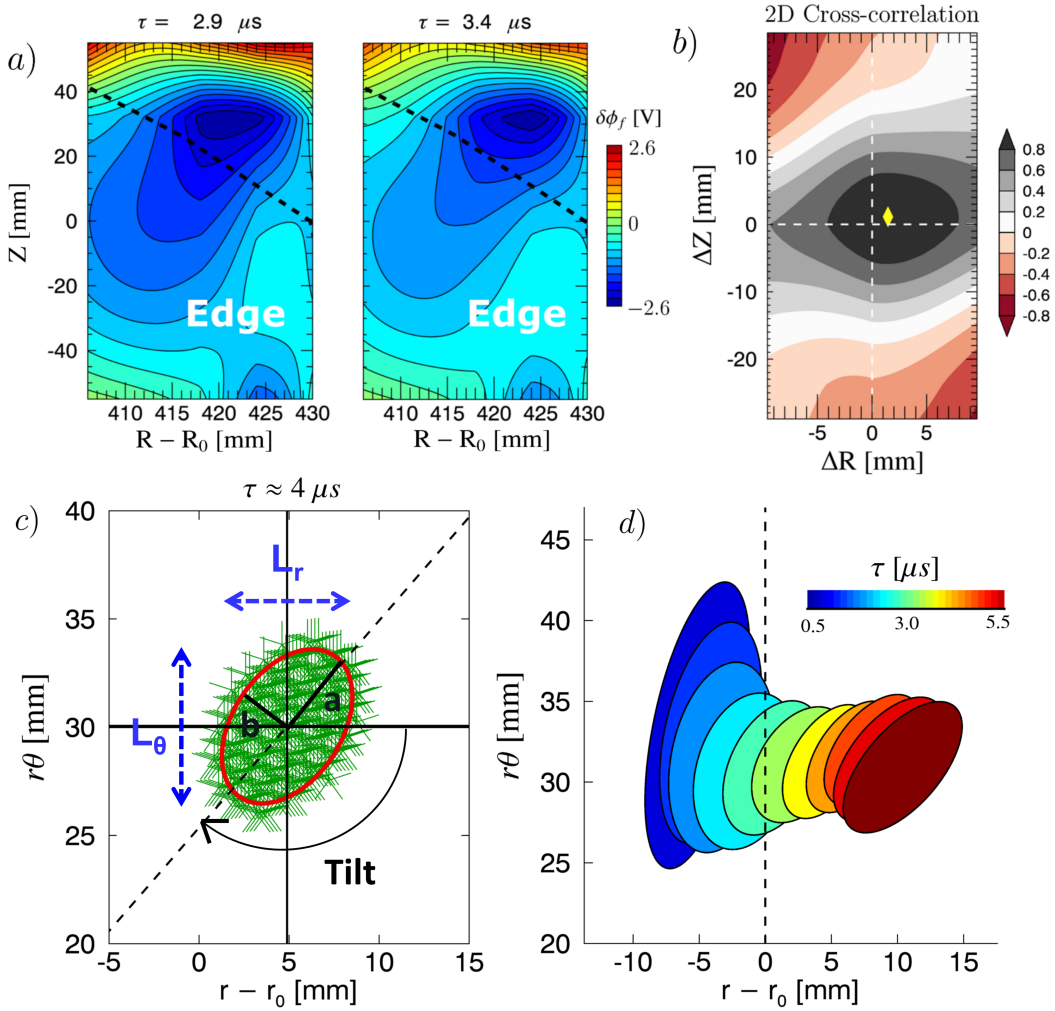


**Figure 9.** a) Two subsequent frames of the  $\delta\phi_f$  maps and b) the corresponding 2D cross-correlation between them in L-mode. The yellow diamond symbol indicates the maximum 2D CC, which provides the spatial displacement of the potential structure between the two frames. c) The points within the filament that satisfy 2D AC  $> 0.8$  are fitted by an ellipse with a major radius  $a$  and minor radius  $b$ . The tilt is defined as the angle to radial direction clockwise, while the radial and poloidal blob sizes are defined as the maximum blob projection over the radial and poloidal direction, respectively. d) Fitted ellipses over time propagating from the edge to the SOL.

thus a factor:  $\sqrt{\log(0.8)/\log(0.5)}$  in size obtained at 0.8 threshold. The ellipse curve in red line represents the fit of data considering the parameters obtained from the eigendecomposition of the covariance matrix (the points that satisfy the threshold), showing a tilted ellipse with respect to the radial axes. Fig. 9 d) shows the outcome of ten fitted blobs in subsequent time frames. In the edge, at the vicinity of the LCFS, the structure is mainly elongated in the poloidal direction but, as it travels radially outward, the tilt increases and its shape approaches a circle, becoming stretched slightly again further outside.

The described technique permits to calculate some filament cross-field parameters,

such as size, shape, and velocity along its trajectory. Fig. 10 shows the filament: a) radial ( $L_r$ ) and b) poloidal ( $L_\theta$ ) sizes, c) ratio between the poloidal and radial sizes ( $L_\theta/L_r$ ), d) potential amplitude (minimum of potential,  $\delta\phi_f^{min}$ ), e) radial velocity ( $v_r$ ), and e) poloidal velocity ( $v_\theta$ ) from the edge to the SOL for the three reference shots shown in Fig. 2. These parameters were calculated in 50 ms time slices within the time window: 470-570 ms, during L-mode, with 50% of overlap. The plotted results correspond to the ensemble average over the sub-time windows, with their error defined as the standard deviation. Besides, the thick black line and the grey area correspond to, respectively, the mean and standard deviation of the corresponding parameter over the three considered shots, further increasing the statistical significance of the result. Note that this procedure provides the most likely filament shape and size over the most probable trajectory, while the error is aimed to account for the dispersion of the blob population detected with the threshold criterion. In the plasma edge ( $r - r_0 < 0$ ), the detected potential blob is more elongated over the poloidal direction than in the radial one ( $L_\theta/L_r > 1$ ), while further outside in the SOL ( $r - r_0 > 0$ ), they become comparable ( $L_\theta/L_r \approx 1$ ). Besides, blobs detected in the near edge rotate in the electron diamagnetic direction,  $v_D^e = -\hat{\mathbf{b}} \times \nabla p_e / (en_e B)$ , where  $\hat{\mathbf{b}} = \mathbf{B}/B$ , in the same direction of the background  $E \times B$  poloidal flow. The transition to the SOL is characterized by an increase of the radial velocity near the LCFS that gradually decreases in the SOL. Along this process, the poloidal velocity flips sign, and the negative potential becomes further enhanced.

The blob tilt and ellipticity emerge from the competition between turbulence drive and saturation that, in turn, are strongly affected by magnetic shear, and  $E \times B$  shear flows [35, 25]. Blob cross-field distortion can, under certain condition, induce stress [25, 3], while the enhancement or not of the background flow might depend on the blob tilt orientation [36]. Fig. 11 shows the blob: a) tilt angle with respect to the radial direction (clockwise, Fig. 9 c), b) ellipticity (defined as the ratio between the major by the minor axes of the fitted ellipse Fig. 9 c), c) area ( $\pi ab$ , where  $a$  and  $b$  are the major and minor radius of the fitted ellipse), and d) vorticity. The tilt significantly changes when the filament crosses the separatrix. While in the near edge the structure is mainly aligned poloidally, in the SOL the tilt saturates around  $140^\circ$ . The ellipticity slightly varies along the trajectory, with higher values in the edge. Fig. 11 c) shows that the effective blob area reduces as the filament travels towards the SOL. The variation of blob area along its trajectory, related to the compactness factor defined elsewhere [58], suggests an intense blob-background interaction in the SOL leading to the lost or spread of the initial blob area. Lastly, the blob parallel vorticity ( $\omega_{\parallel} = (\nabla \times \mathbf{v})_{\parallel} \sim \nabla_{\perp}^2 \phi_f / B$ ) is shown in Fig. 11 d). The absolute vorticity value is lower in the edge, around  $0.1 \times 10^6 \text{ s}^{-1}$ , becoming higher in the SOL, where it reaches values around  $0.4 \times 10^6 \text{ s}^{-1}$ .

As discussed before, the external electrode biasing can enhance the background  $E \times B$  shear flow around the LCFS (Fig. 4 d), resulting in the partial suppression of turbulence [41] and the steepness of the density profile. In addition, we have seen (Fig. 6) that the effective turbulence radial correlation length strongly reduces in the SOL during

## L-mode

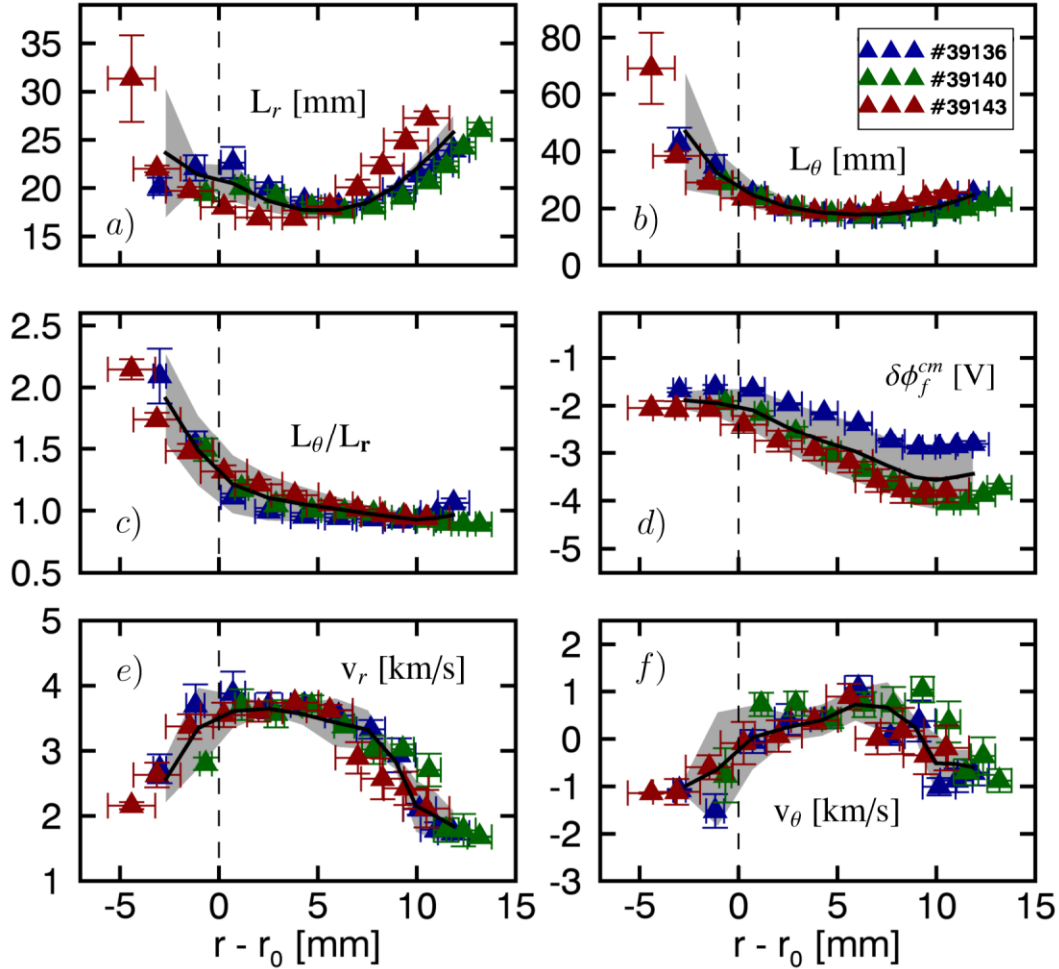


**Figure 10.** Filament parameters as a function of the radial position from the edge to the SOL in L-mode. The plots show filament a) radial size, b) poloidal size, c) ratio between the poloidal and radial size, d) blob potential amplitude, e) radial velocity, and f) poloidal velocity. The full black line indicates the average of the parameter over the three considered shots (Fig. 2) and the grey area, the corresponding standard deviation.

biasing, while the  $I_s$  blob obtained from the conditional average is substantially different in L and H-mode (Fig. 7 c) and d)). To investigate the impact of H-mode regime, and of the associated occurrence of strongly sheared poloidal flow, on the dynamics of turbulent filaments in the plasma boundary, the two-dimension conditional average floating potential is again employed. The reference is the same  $I_s$  signal in the SOL shown in Fig. 7 d). Fig. 12 shows the blob floating potential structure in thirty-two frames. The reference  $I_s$  position is represented by a small red circle displayed in the near SOL, together with two other  $I_s$  signals (innermost - black, outermost - blue). The white arrows depict the  $E \times B$  flow direction and strength, obtained from the floating potential map. One can see in the first frames a dipole structure building up

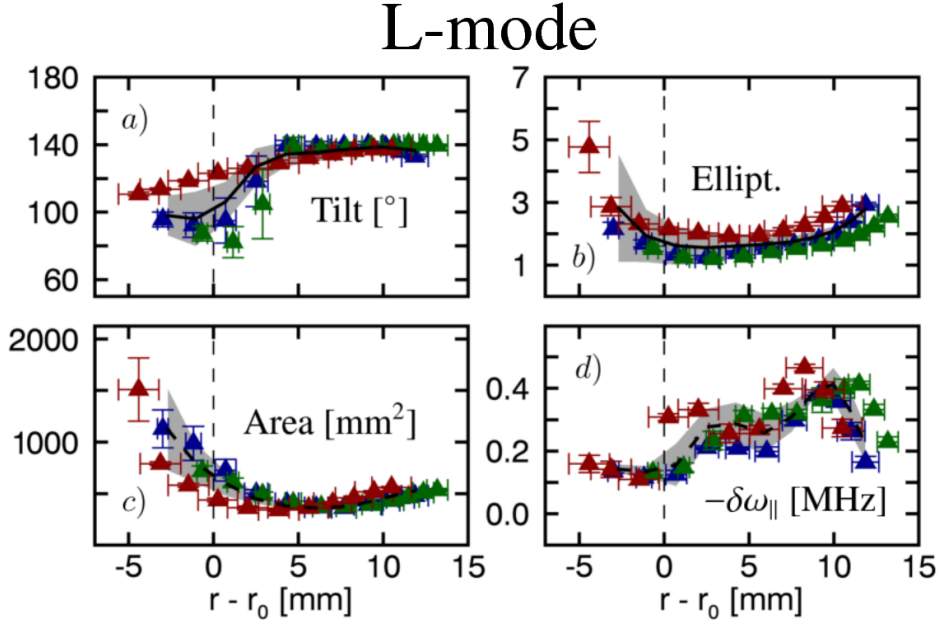


**Figure 11.** Filament a) tilt angle (clockwise), b) ellipticity, c) area, and d) vorticity in L-mode as a function of the radial position. The full black line indicates the average of the parameter over the three considered shots (Fig. 2) and the grey area, the corresponding standard deviation.

around the LCFS. At  $\tau = 0$ , i.e., when the reference  $I_s$  peaks (Fig. 7 d), an unbalanced dipole structure rather aligned poloidally than radially is observed. In the subsequent frames, the structure becomes spread radially over almost the whole R interval. Its minimum, however, lies roughly at the middle distance between the vertical borders of the frame. Later on, the structure slows down, remaining roughly at the same position at  $\tau = 2 \mu s$ . One might argue that the structure becomes trapped in this region. Besides, its amplitude gradually reduces to zero, suggesting its depletion. Interestingly, the vortex  $E \times B$  flow becomes more pronounced when the structure is in the SOL before the structure fades away. Differently from Fig. 8, where the potential structure resembles an ellipse in the cross-field plane, in Fig. 12 a finger-like structure is more evident. This result is similar, at least qualitatively, to the high-temperature filaments observed during the ELM-cycle in the KSTAR tokamak [59]. One might speculate that the inter-ELM filaments observed in RFX-mod are likely in an intermediate regime where filaments are hotter than those in L-mode, but the background  $E \times B$  shear still deeply impacts their dynamics [60].

The statistically evaluated filament parameters for H-mode are shown in Fig. 13. Analogously to Fig. 10, it is shown the blob a) radial and b) poloidal sizes, c) the ration between the poloidal and radial size, d) the minimum potential amplitude, and the blob e) radial and f) poloidal velocities for the three reference shots (Fig. 2). The analysis was carried out in a time window of 100 ms during H-mode. The final result is obtained from the ensemble average over 50 ms sub-time windows with 50% overlap,

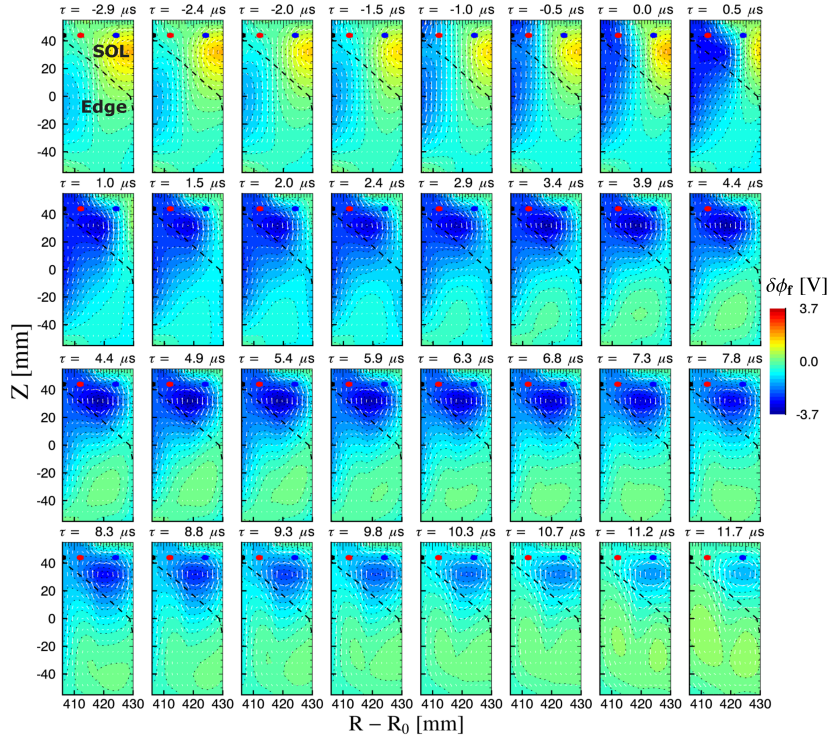


**Figure 12.** Conditional average of filaments detected with the threshold criterion during H-mode as seen from a 2D floating potential map in thirty-two frames (#39136). The white arrows represent the  $E \times B$  flow.

with the error given by the ensemble standard deviation. Since blobs become well defined in the frames when they are already in the SOL (approximately from  $\tau = 0$  on), we restricted our analysis to that range in H-mode. Note that this differs from L-mode where blobs are already visible in the confinement region, i.e., their centre of mass is within the observation frame, which is important to avoid misinterpretation of their size and shape. At the same time, their amplitude does not change appreciably in-between frames, satisfying the criterion of maximum cross-correlation larger than 0.8. The mentioned trapping effect is confirmed from Fig. 13 e) and f). Near the LCFS, the detected structure exhibits a higher radial and poloidal velocity (in the ion diamagnetic direction,  $v_D^i = \hat{\mathbf{b}} \times \nabla p_e / (en_e B)$ ). Further out in the SOL, both  $v_r$  and  $v_\theta$  reduce nearly to zero. The poloidal size is larger than the radial one near to the LCFS, meaning that the structure is poloidally elongated in this range. The poloidal velocity is in the ion diamagnetic direction in this case, opposite to  $v_\theta^{E \times B}$ . Lastly, the fast reduction of the structure amplitude (Fig. 13 d) near the region where it becomes trapped suggests its depletion.

Fig. 14 shows the blob: a) tilt angle with respect to the radial direction (clockwise), b) ellipticity, c) cross-field area, and d) vorticity, calculated at the center of mass of the negative pole, during H-mode. The tilt angle in Fig. 14 a) supports the claim that the structure is poloidally aligned near the LCFS, while the large ellipticity suggests its

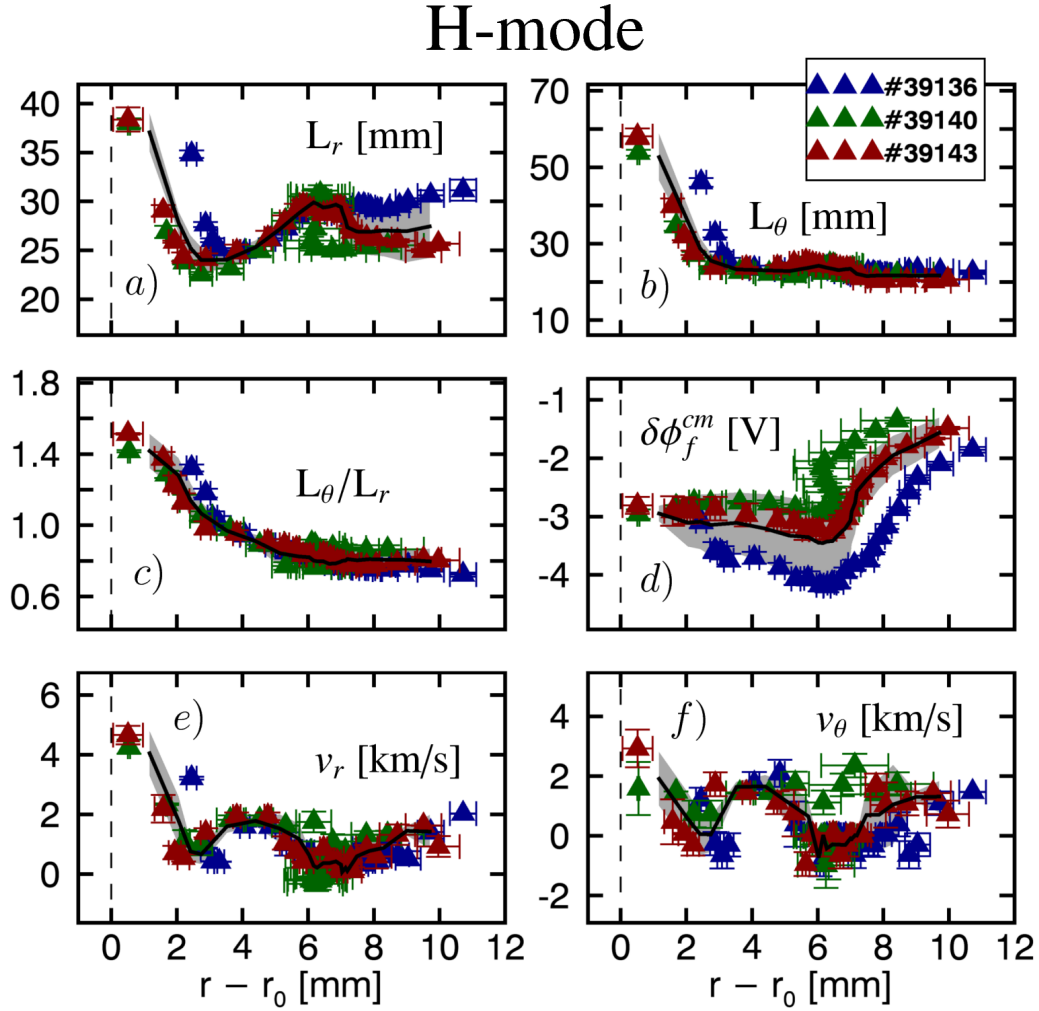


**Figure 13.** Filament parameters as a function of the radial position from the edge to the SOL in H-mode for the reference shots (Fig. 2). The plots show filament a) radial size, b) poloidal size, c) ratio between the poloidal and radial size, d) blob potential amplitude, e) radial velocity, and f) poloidal velocity. The full black line indicates the average of the parameter over the three considered shots (Fig. 2) and the grey area, the corresponding standard deviation.

stretching (Fig. 14 b). In the trap region, the structure becomes less tilted poloidally, while the ellipticity approaches 2. Concomitantly, the amplitude decreases sharply (Fig. 14 d), indicating that the structure is depleted in this region. The vorticity (Fig. 14 d) becomes higher in the trap region and drops sharply when the potential amplitude approaches zero, roughly following the variations of the blob area (Fig. 14 c).

### 3.3. The impact of background $E \times B$ shear flows on blob dynamics

Blobs are expected to be destroyed by high enough cross-field shear flows as predicted by analytical models [29] and observed in simulations [8]. According to [27], streamers, radial elongated turbulence structure, or blobs can be torn apart by an external  $E \times B$

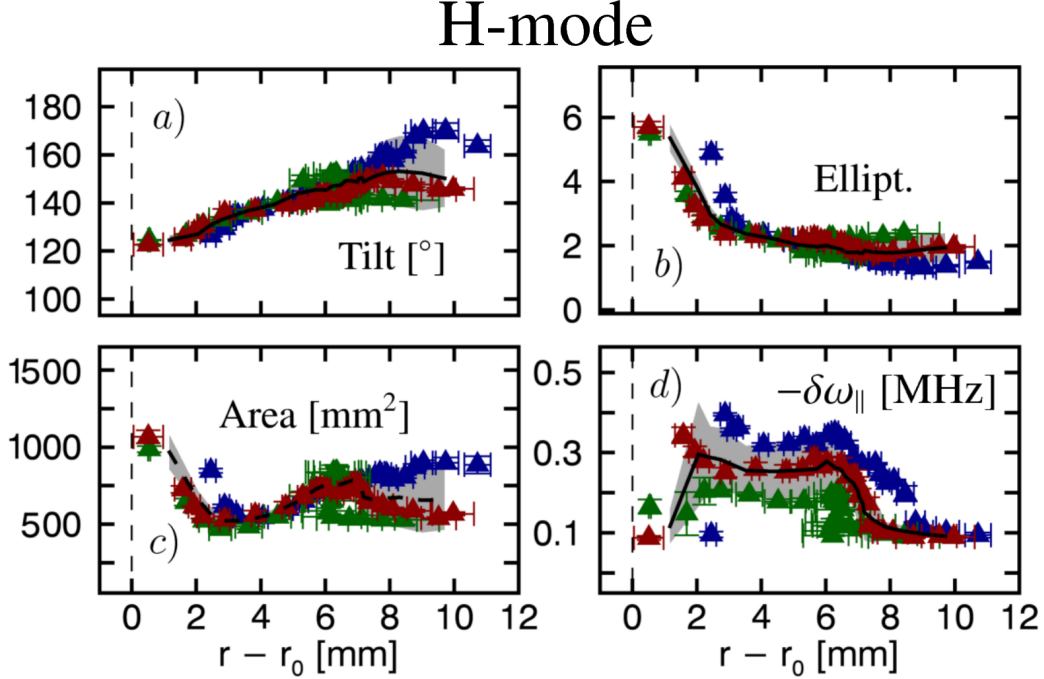


**Figure 14.** Filament a) tilt angle (clockwise), b) ellipticity, c) area, and d) vorticity as a function of the radial position in H-mode. The full black line indicates the average of the parameter over the three considered shots (Fig. 2) and the grey area, the corresponding standard deviation.

flow if their convective time,  $\tau^{blob} = L_r/(|v_r|)$ , is larger than the shear decorrelation time,  $L_\theta/(L_r|\gamma^{E \times B}|)$ , where  $\gamma_{E \times B} \cong B^{-1}dE_r/dr$ . The background shear, therefore, imposes a limit for what kind of structure survives: slower and/or bigger blobs are likely to be ripped apart by it. This approach is analogous to the well-known eddy decorrelation criterion [61]. To test whether this criterion can be applied to the present experiment, the  $E \times B$  shearing rate was estimated from the floating potential ( $\gamma_{E \times B} \approx B^{-1}d^2\phi_f/dr^2$ ) around the range where filaments are detected. Fig. 15 a) compares the shearing rate profile in L-mode with the inverse of the effective turbulent characteristic time ( $1/\tau^{turb} = v_r L_\theta/L_r^2$ ). The blue dashed line represents  $\gamma_{E \times B}$  during L-mode, while the triangles represent  $1/\tau^{turb}$ . Both curves are the result of the average over the three considered shots (Fig. 2). The most likely filament in L-mode (blue points) exhibits  $1/\tau^{turb}$  higher than the background shear along its trajectory. Only in the outer regions, they become comparable. Therefore, according to the suppression criterion [27], L-mode filaments are expected to withstand the background  $E \times B$  shear. Fig. 15 b) shows the same situation now in H-mode, with  $1/\tau^{turb}$  represented by down triangles and  $\gamma_{E \times B}$  by the dashed line in red. Note that in this case, the shear flow increases above the limit where the L-mode blobs are expected to survive. The detected filaments have  $1/\tau^{turb}$  below  $\gamma_{E \times B}$  over their entire trajectory. Although filaments do not radially propagate in this regime as in L-mode, the potential structure remains (trapped) for a relatively long period in the SOL before fading away. Therefore, the potential structure is not

instantaneously suppressed as the criterion might suggest. A clear visual distinction between L and H-mode is the presence of a monopole potential in the latter. Since the  $E \times B$  drift is an essential ingredient for the blob motion, an unbalanced dipole or monopole potential would lead the blob to spin rather than propagate radially. The presence of a monopole or unbalanced potential is also expected when the blob has a temperature higher than the surrounding background plasma [60, 62]. In addition, studies of vortex structures embedded in a background sheared flow indicate that while a 'prograde' vortex, i.e., when its vorticity has the same sign of the background shear, is stable, an 'adverse' vortex, i.e., when they have opposite sign, is unstable and tends to fragment [63]. Therefore, the background shear selects vortices based on the sign of their vorticity. In magnetized plasmas, this effect has been pointed out to be responsible for changing the relative population of the positive and negative potential pole in the plasma edge [64]. This effect can ultimately modify the turbulent transport properties in regions where coherent structures exist, with superdiffusion transport where the population of dipolar vortex structure is dominant [65], and subdiffusion where monopolar structure population is surplus [66]. Besides, in certain conditions, a vortex can feed the background shear or be fed by it, resulting in its depletion in some cases, while background shear gets enhanced by enstrophy transfer [36]. The monopole vorticity in H-mode (Fig. 14 d) has the same sign of the background shear in the near SOL (Fig. 4 d), suggesting that the vortex is 'prograde'. The positive vortex that supposedly should be unstable in this region does not appear in the frame. This result is in qualitative agreement with the vortex selection criterion. Further outside, the shear becomes positive, and so the potential blob becomes 'adverse' which supports its depletion. In L-mode, the shearing rate is lower than the blob vorticity (Fig. 11 d), which might be the reason why the potential blob is not so affected [67].

In the light of these results, we conclude that the reduced turbulence activity in the SOL observed in H-mode is mainly driven by the stronger  $E \times B$  shear flows in this regime. Two mechanisms are the main candidates for that: 1) blob decorrelation [27]; 2) vortex selection by background  $E \times B$  shear flows that leads to trapping [60] until its depletion.

#### *3.4. Filaments: magnetic fluctuations*

The U-probe was designed to measure simultaneously electrostatic and magnetic fluctuation. In the RFX-mod operating in the RFP configuration, this probe has been used to study electromagnetic filaments [68]. Parallel current density structures related to plasma density blobs were observed in tokamaks and stellarators [69, 70], and during edge-localized mode (ELM) events [71, 72]. While those measurements are typically restricted to 0D or 1D, in the TORPEX device, 2D maps of the parallel current density were computed [73], showing a good agreement with analytical predictions [6].

In the scrape-off layer region of fusion devices, the magnetic field lines intercept a material surface, opening a channel of parallel dissipation. A simple electrostatic cold

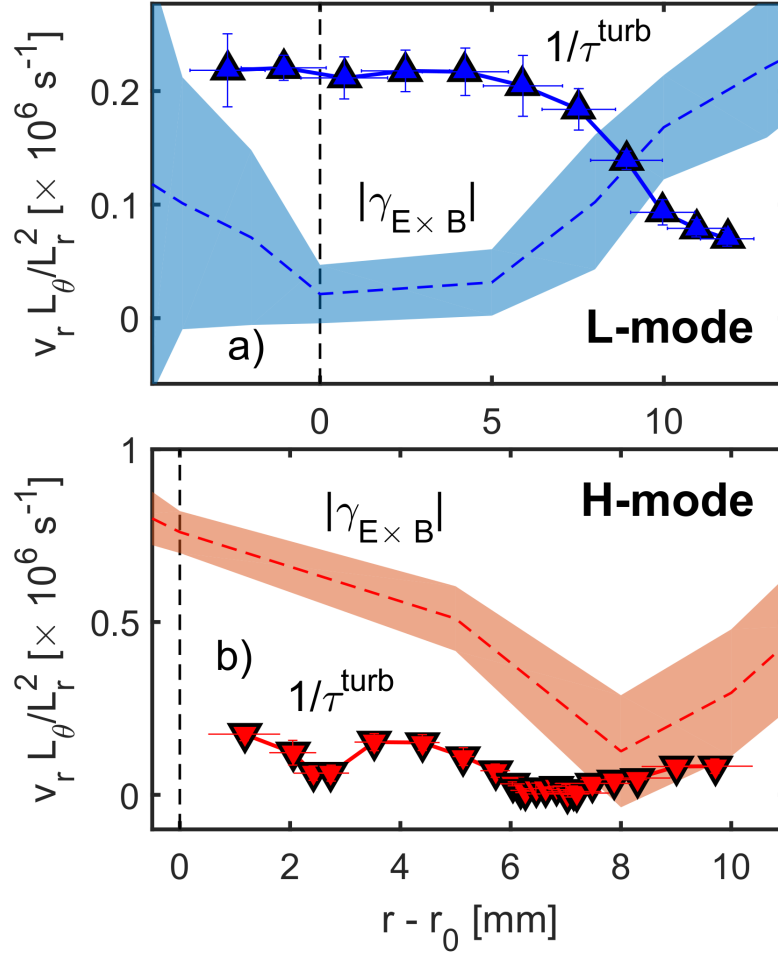


**Figure 15.** Comparison of the  $E \times B$  shearing rate with the blob effective time ( $v_r L_\theta / L_r^2$ ) in L-mode and H-mode. The parameters are result of the average over three shots (#39136, #39140 and #39143). The dashed lines represent  $\gamma_{E \times B}$ , while the triangles the blob inverse of the effective characteristic time ( $1/\tau^{\text{turb}} = v_r L_\theta / L_r^2$ ).

ion filament model [6] can be deduced from charge conservation ( $\nabla \cdot \mathbf{j} = 0$ ), where an effective gravity force  $\mathbf{F}$  acts as a source of polarization current perpendicular to the local magnetic field. As a response to that, a parallel current density is developed to dissipate it. Besides, the ions inertia results in the polarization drift perpendicular to the magnetic field. The vorticity equation describes the combination of all these terms:

$$\nabla \cdot \frac{d}{dt} \left( \frac{nm_i}{B^2} \nabla_\perp \phi \right) = \nabla_\parallel j_\parallel + \frac{1}{B} \mathbf{b} \cdot \nabla \times \mathbf{F} \quad (4)$$

where  $\phi$  is the electrostatic potential,  $n$  is the plasma density,  $B$  is the magnetic field,  $m_i$  is the ion mass,  $j_\parallel$  is the parallel current density,  $\mathbf{b} = \mathbf{B}/B$ , and  $d/dt = \partial/\partial t + \mathbf{v}^{\mathbf{E} \times \mathbf{B}} \cdot \nabla$ , where  $\mathbf{v}^{\mathbf{E} \times \mathbf{B}} = (\mathbf{b} \times \nabla \phi)/B$ . This equation provides a mechanism whereby filaments are propelled and dissipated. Similarly, a simple equation for the density blob can be obtained from the continuity equation considering sources and sinks [6]. The density

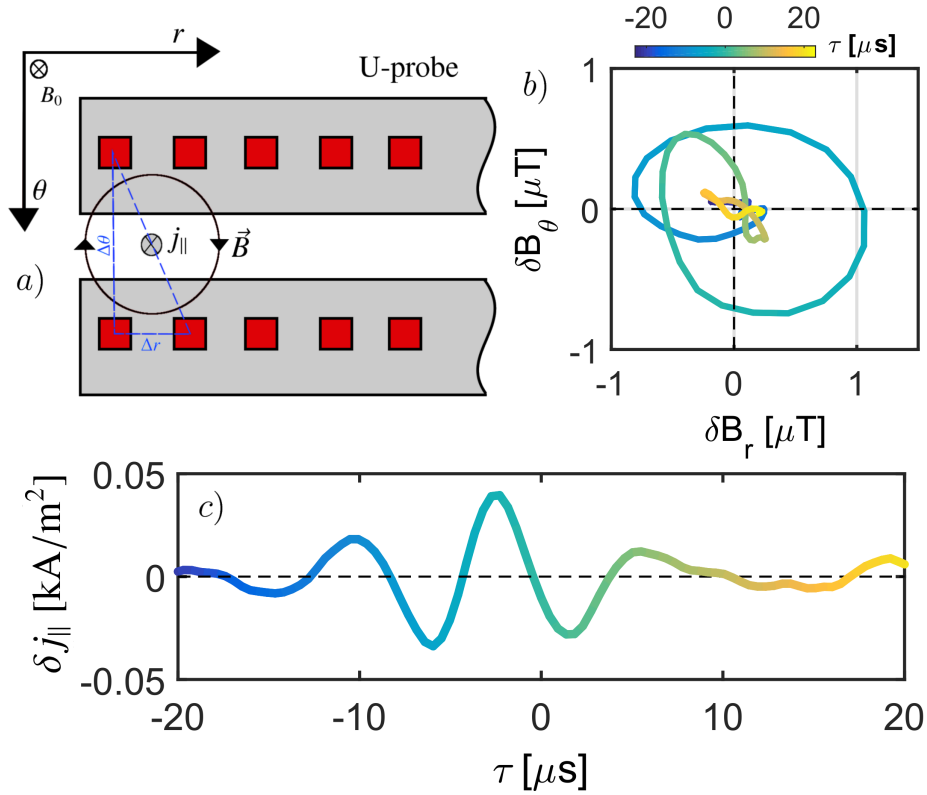


**Figure 16.** Magnetic features of conditional averaged filaments in L-mode. a) Cartoon showing the magnetic sensors in each tower of U-probe (in red). At least three coils poloidally and radially displaced are necessary to evaluate the parallel current density. b) hodogram of the poloidal vs radial magnetic field fluctuation, and c) parallel current density (#39136).

blob travels with  $\mathbf{v}^{\mathbf{E} \times \mathbf{B}}$ , which, in turn, is fed by the vorticity equation, thus making the two equations coupled.

Different filament regimes arise from the closure current path [11]. If the current flows into a material surface, e.g., the divertor plates, without any further disturb, the two terms on the left-hand-side (LHS) of (4) dominate over the ion polarization drift term on the RHS. This regime is called sheath-limited (SL). The parallel current density at the closure region is typically given by Bohm's boundary condition:  $j_{\parallel} = j_s [1 - \exp(-e\phi_f/T_e)]$  [55], where  $j_s \approx 0.6n_0ec_s$  [15] is the ion saturation current density at the sheath, where  $c_s \approx \sqrt{T_e/m_i}$  is the sound speed and  $n_0$  is the plasma density far from the sheath. However, if the collisionality along the field lines ( $\nu_{\parallel}^* \propto nT^{-2}$ ) increases over a certain limit, the parallel conductivity can drop and then the ion polarization drift might overcome the parallel term, balancing with the charge polarization one. In this regime, called inertial (IN), the filament is electrically disconnected from the divertor or any material surface [11]. Further effects, such as the magnetic 'fanning factor' near the X-point [74] and ion-neutral collisions [75] might also affect the filament dynamics, e.g., by enhancing the perpendicular current. A more general model takes

into account the ion finite temperature [76], which is likely the case for the SOL of fusion devices [77, 78]. In addition, electromagnetic effects start becoming important typically when  $\beta > (m_e/m_i)$ , where  $\beta = n_e T_e / (B^2 / 2\mu_0)$ . In such a regime, filaments can lead to field line bending and to an alternative current closure [6].

With a set of magnetic sensors installed in each tower of U-probe (Fig. 1), we can measure simultaneously  $\dot{B}_r$ ,  $\dot{B}_\theta$  and  $\dot{B}_t$ , where the 'dot' stands for the time derivative. The sensors are arranged radially and poloidally. From the Ampere's Law, the parallel current density can be obtained from the magnetic field,  $j_{\parallel} \approx 1/\mu_0 [\partial_r B_\theta - \partial_\theta B_r]$ , in the slab geometry approximation. This method has been applied to measure plasmas in the magnetosphere [79] and used for the first time in fusion plasmas in RFX-mod [80]. Fig. 16 shows an example of magnetic perturbations related to the  $I_s$  conditional averaged blobs in the SOL during L-mode (same reference as Fig. 7). The local poloidal and radial magnetic field amplitude combined with their relative cross-phase yields a circle shape depicted in the hodogram of Fig. 16 b). The corresponding parallel current density is shown in Fig. 16 c), with the maximum value occurring right before the  $I_s$  peak (zero delay): this non-synchronization is not surprising since they are radially-poloidally displaced. The parallel current density exhibits both positive and negative oscillation throughout the time window, which is a signature of a multipolar structure. Similar behaviour has been observed within an ELM-cycle in the COMPASS tokamak [72]. The maximum parallel current density estimated by conditional averaging blobs in L and H-mode are  $|\delta j_{\parallel}^L| \approx 0.04$  kA/m<sup>2</sup> and  $|\delta j_{\parallel}^H| \approx 0.1$  kA/m<sup>2</sup>, respectively. Considering that the current density structure has the same size as the potential one (as observed in [55]), and using the negative pole area from Fig. 11 c) just outside the confinement region, i.e.,  $\text{Area}^L \approx 500$  mm<sup>2</sup>, we see that filaments in L-mode can carry a current of  $I^L = |\delta j_{\parallel}^L| * \text{Area}^L \approx 20$  mA, where it was assumed that parallel current density is uniform over the blob area. Likewise in H-mode, assuming an  $\text{Area}^H \approx 750$  mm<sup>2</sup> (from Fig. 14 c), the current carry by filaments is  $I^H \approx 70$  mA.

Considering blob parameters around the LCFS, we can compute the contribution of current flowing to the sheath neglecting the plasma resistivity along the field lines. In L-mode:  $|\delta j_{\parallel}^L| / (0.6 n e c_s (1 - \exp(-e\delta\phi_f^L/T_e))) \sim 0.2$ , where it was used  $\delta\phi_f^L \approx 2$  V (Fig. 10 d),  $T_e^L \sim 15$  eV, where  $n$  and  $c_s$  are time averaged values in L-mode. This result suggests that the resistivity along the field lines is not negligible. Following the same procedure for H-mode now, the sheath contribution for this regime is  $|\delta j_{\parallel}^H| / (0.6 n e c_s (1 - \exp(-e\delta\phi_f^H/T_e))) \sim 0.2$ , i.e., similar to L-mode; here  $\delta\phi_f^H \approx 3$  V (Fig. 13 d),  $T_e^H \sim 10$  eV. Assuming that the resistivity along the field lines is given by the Spitzer electrical resistivity  $\rho_{\parallel}^{\text{Spitzer}} \propto T_e^{-3/2}$  [15], one can notice that this quantity is expected to be higher in H-mode. Therefore, to sustain the total current in this regime, one can expect a larger current dissipation perpendicularly to the magnetic field, possibly through ion polarization or collisional currents [6].

The two-dimension array of 3-axial coils was exploited to obtain the  $j_{\parallel}$  cross-field map by combining the signals from the two towers in groups of three sensors, radially and poloidally displaced, as shown in Fig. 16 a). The position of each combination is

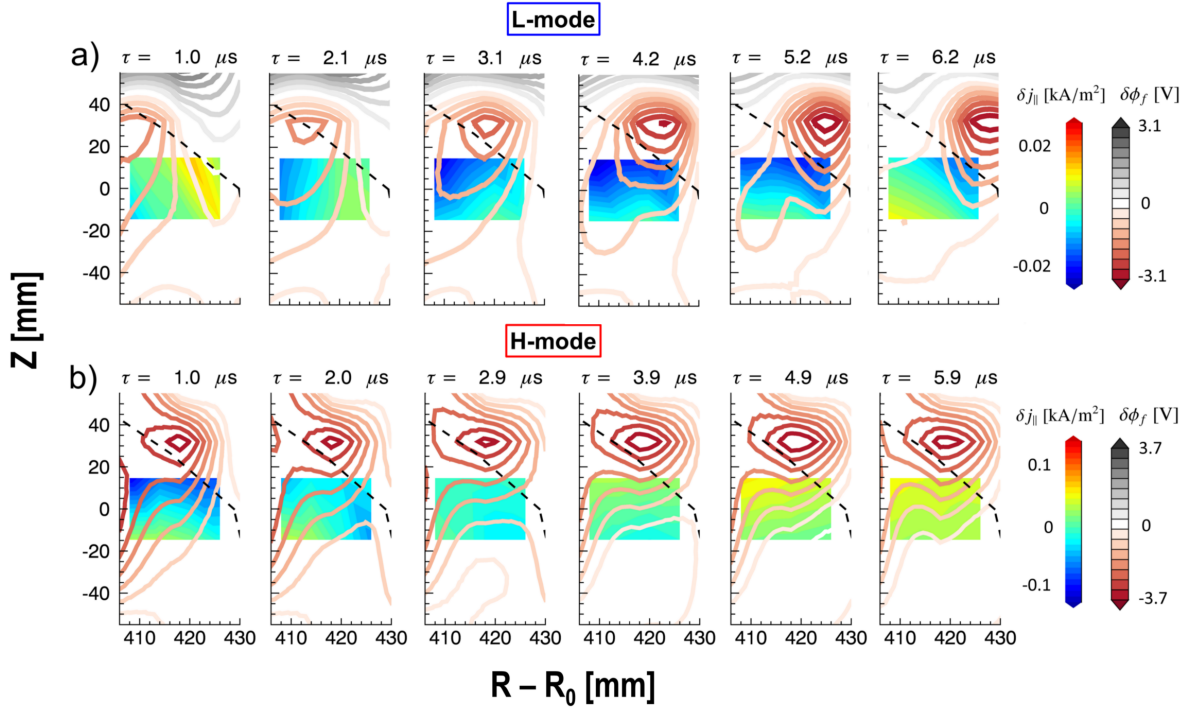


**Figure 17.** Conditional averaged parallel current density ( $\delta j_{\parallel}$ ) map during L-mode (top) and H-mode (bottom) related to the same  $I_s$  references shown in Fig. 7 c) and d), respectively. The contours overplotted represent the conditional averaged floating potential ( $\delta\phi_f$ ) as shown in Fig. 8 and Fig. 12 (#39136).

the barycenter of the triangle formed by the three coils. The map is built from a total of five magnetic sensors in each tower, resulting in a  $4 \times 2$  radial-poloidal grid. Fig. 17 shows the 2D map of  $j_{\parallel}$  associated to the same  $I_s$  references shown in Fig. 7, for L and H-mode, through conditional average. In addition, the blob floating potential map in each scenario was overplotted. During L-mode (Fig. 17, top panel), the  $j_{\parallel}$  evolution seems to be closely related to the propagation of the floating potential structure. Both show an almost synchronized negative structure that propagates radially outward from the edge to the SOL. The result is, at least qualitatively, in agreement with the sheath-connected regime [55, 81], where parallel transport along the magnetic field lines through a sheath is the dominant filament dissipation mechanism. During H-mode (Fig. 17, bottom panel), the parallel current density becomes larger, as expected for a higher beta environment [69]. In the first frame,  $j_{\parallel}$  reaches the largest absolute value, spreading over the edge up to the near SOL. In the second frame, the  $j_{\parallel}$  structure becomes more restricted to a narrower range in the edge. In the subsequent frames, the parallel current density strongly reduces while the structure becomes trapped in the near SOL. The result suggests that blobs in H-mode arise with larger parallel current density compared to those in L-mode, in the proximity of the plasma boundary, but it becomes lower in the SOL.

### 3.5. Scaling blob velocity with its size

The filament dynamic depends on different plasma parameters, e.g., the level of collisionality along the field lines and the magnetic topology [60, 6]. They ultimately determine whether filaments at the outboard midplane are or not electrically connected to a material surface elsewhere, e.g., divertor tiles or the wall [78]. As predicted by the two-region model [11], the connection between these two regions is expected to impact the filament cross-field velocity and size. As discussed in the previous section, in the sheath connected or sheath-limited (SL) regime, the parallel dissipation is predominately along the field lines toward the sheath of a material surface. On the opposite direction, in the resistive ballooning or inertial (IN) regime the two regions become electrically disconnected due to the higher parallel resistivity along the field lines and so the closure of the current (assuring quasineutrality  $\nabla \cdot \mathbf{j} = 0$ ) is provided by the ion polarization drift. These two regimes set, respectively, a lower and an upper boundary for the blob velocity scaling in the cold ion approximation. The filament velocity in these two regimes are [7]:

$$v_b^{SL} = 2c_s \frac{L_{\parallel}}{R} \left( \frac{\rho_s}{\delta_b} \right)^2 \quad (5)$$

$$v_b^{IN} = c_s \sqrt{2 \frac{\delta_b}{R}} \quad (6)$$

where  $\delta_b$  is the blob size,  $\rho_s = \sqrt{T_e m_i} / eB$  is the ion sound gyroradius, and  $L_{\parallel}$  is the parallel connection length defined as the length of the magnetic field in the SOL. The transition between these two regimes is controlled by the effective collisionality  $\Lambda = \nu_{ei} L_{\parallel} / (\Omega_e \rho_s)$  [11], where  $\nu_{ei}$  is the electron-ion collision frequency and  $\Omega_e$  is the electron gyrofrequency.

When finite ion temperature and electromagnetic effects are taken into account, new filament regimes arise [76]. The finite magnetic inductance in the parallel direction from the Ohmic's law [54] when  $\beta = (c_s/v_A)^2 > m_e/m_i$  leads to the propagation of Alfvén-waves that dissipate the charge building up, where  $v_A$  is the Alfvén velocity [6]. The biasing L-H transition in RFX-mod running as a tokamak is followed by an increase of  $\beta$  in the plasma edge (mainly due to an increase in the density) from  $\beta^L \sim 3 \times 10^{-5}$  to  $\beta^H \sim 6 \times 10^{-5}$ ; still, lower than  $m_e/m_i$ , i.e., electromagnetic effects are likely negligible.

Owing to the plasma-wall proximity, we devoted some effort to properly evaluate the parallel connection length since it is a crucial parameter for characterizing coherent structures in the SOL. On this purpose, the full equilibrium reconstruction was computed considering a free boundary version of the IET code [82]. In order to get an accurate equilibrium reconstruction, the estimation of IET free parameters was performed by using an iterative scheme trying to minimize the discrepancy between the

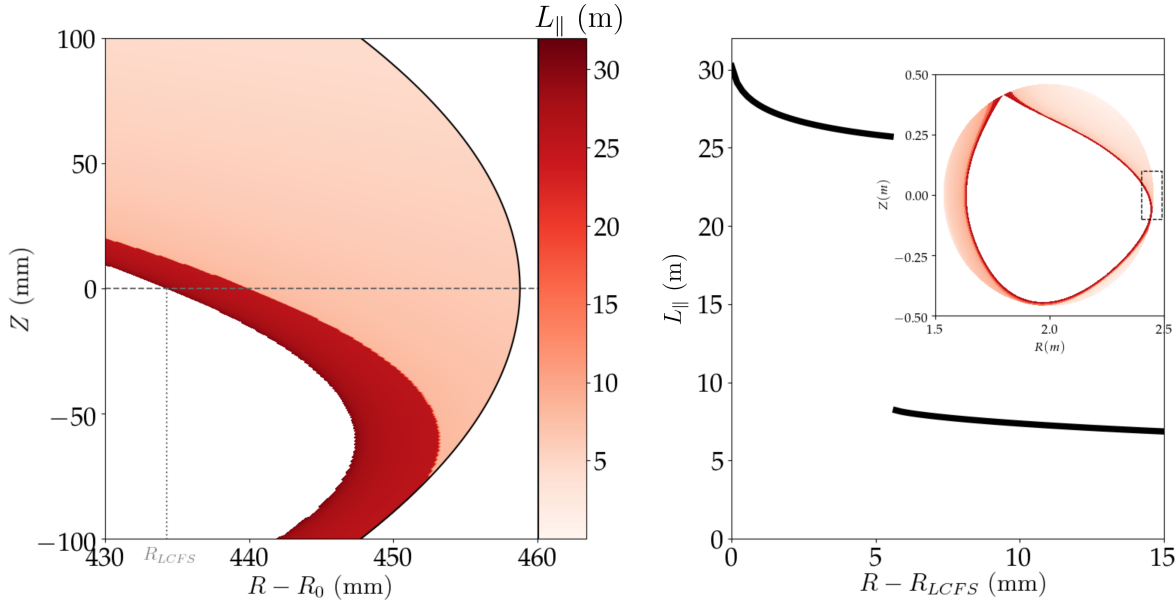


**Figure 18.** On the left, parallel connection length ( $L_{\parallel}$ , the sum of backward and forward field line integration) shown in a 2D map in the region where the U-probe was inserted. On the right,  $L_{\parallel}$  radial profile at the outboard midplane together with full cross-section reconstruction (small chart); the small rectangle indicates the region where the U-probe was inserted.

poloidal magnetic field experimentally measured by pick-up coils and the one simulated by the model [83]. The magnetic boundary is in a good agreement with the real-time boundary reconstruction [47], with less than 1 cm of discrepancy at the outboard midplane. Starting from the magnetic flux surface reconstruction obtained with the method described [84], the parallel connection length was then calculated using the field line integration code NEMATO [85]. The connection length is obtained by the sum of the backward and forward line field integration, starting from a reference point in the SOL. This procedure is done iteratively over the entire cross-field section, and the result is shown in Fig. 18. The map on the left of Fig. 18 shows a zoom-in of the cross-section range where the U-probe was inserted. The connection length values vary from a few centimetres up to 50 m, dark to light red, respectively, according to the colour scheme. The radial profile of the connection length at  $Z = 0$  is presented on the right side of Fig. 18, while the small chart shows the  $L_{\parallel}$  map over the full poloidal section. One can identify two distinct regions. While near the separatrix  $L_{\parallel}$  is larger, and the field lines are connected to the strike points at the top vessel. Further out, the connection length drops significantly in the limiter shadow region. The field lines in this region become connected to the outboard midplane wall. Since the radial range where the transition between the two layers occurs is comparable to the range covered by the probe, it likely affects the observed blob dynamics. Fig. 18 shows the connection length computation for an equilibrium reconstruction in L-mode, while we have not observed any significant variation in H-mode.

Fig. 19 shows the normalized blob radial velocity by the ambient sound speed ( $v_b/c_s \sim v_r/c_s$ ) as function of the blob cross-field radius ( $\delta_b/\rho_s \sim L_\theta/(2\rho_s)$ ) normalized by the ion sound gyroradius for L and H-mode scenario. Here the blob size is obtained from the negative pole of the potential blob, different from previous works where the density or ion saturation blob was used [75, 78, 4]. We note that density/pressure blob can be comparable to the pole of the potential structure as observed experimentally [55, 56]). However, in H-mode, the potential structure tends to become more stretched due to the large  $E \times B$  shear flow [36], and so this comparison might become more difficult. The sheath limit regime (in the cold ion approximation) is represented by the solid and dashed red lines at  $L_\parallel = 10$  m and  $L_\parallel = 30$  m, respectively, i.e., approximately the parallel connection lengths evaluated in the near and far SOL (Fig. 18). We note, however, that the error of the LCFS at the midplane from the magnetic reconstruction [83] might be up to 1 cm; therefore, one has to be careful when comparing Fig. 18 with the blob position in the SOL. The inertial regime is represented by the blue line. They were computed assuming that the electron temperature near the edge is 15 eV in L-mode and 10 eV in H-mode and, hence, the ion sound gyroradius is within the interval  $\rho_s \approx 0.8 - 1.0$  mm, while the sound speed  $c_s = 22 - 27$  km/s.

In L-mode (Fig. 19, left), one can observe that the blobs close the LCFS scale reasonably good as predicted by the sheath connected regime at  $L_\parallel = 30$  m, in fair agreement with the expected connection length in this region. Moreover, blobs detected farther scale better with the sheath connected regime at  $L_\parallel = 10$  m. This result suggests that the blob geometrical centre perceives the variation of the parallel connection length along its trajectory. This result also gives us confidence in the reconstruction of the LCFS. We note that other effects such as the neutral-friction [75] or the magnetic topology around the X-point [6] can also play a role here.

During the ELM-free H-mode phase (Fig. 19, right), blobs near the LCFS seem to scale better as the inertial regime. However, further out, where they become virtually trapped, the better match is with the sheath limited. This result suggests that blobs might become electrically disconnected in H-mode, the parallel current density in this regime (Fig. 17, bottom) is in qualitative agreement with that. Fig. 17 b) shows the effective collisionality ( $\Lambda$ ) close to the LCFS ( $L_\parallel \sim 30$  m) over time. The density here was computed from an  $I_s \propto n_e T_e^{1/2}$  around  $r - r_0 \approx 0$ , while the temperature is evaluated around  $r - r_0 \approx -15$  mm (i.e., in the plasma edge), therefore,  $\Lambda$  is likely underestimated. When biasing is applied,  $\Lambda$  increases sharply, mainly due to a decrease in the electron temperature (Fig. 5 b). Filaments are expected to become disconnected from the target region when  $\Lambda$  increases beyond 1 [11, 78], which agrees with the inertial scale for blobs near the LCFS, and the measured parallel current density in H-mode. Further out, the connection length drops, and so the electrical connection becomes easier to get established. Nevertheless, we note that the role of background shear flows is not foreseen by the model [60]. The interplay between background sheared flows and the blob potential ultimately affects the blob motion (Fig. 12 and Fig. 15) and, therefore, the velocity scaling predictions.

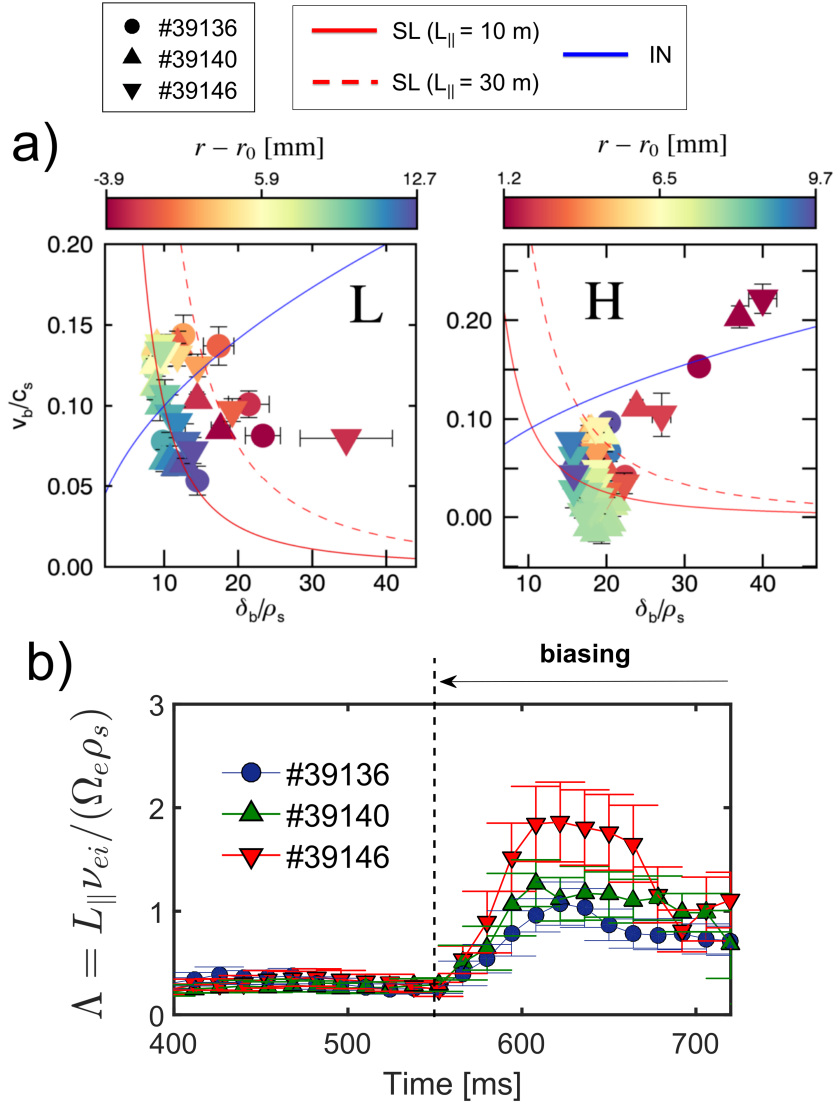


**Figure 19.** a) Blob normalized radial velocity as function of the normalized size in L (on the left) and H-mode (on the right). The symbols represent the three reference shots: circle (#39136), up-triangle (#39140), and down-triangle (#39143). The red lines stands for the sheath limited velocity scale (SL) at  $L_{\parallel} = 10$  m (full line) and  $L_{\parallel} = 30$  m (dashed line). The blue curve represents the inertial scale (IN). The colorbar refers to the position of the detected blob with respect to the LCFS position. b) Effective collisionality around the LCFS over time for the three reference shots (here  $L_{\parallel} = 30$  m).

### 3.6. Filamentary signature close to the wall

The SOL profiles are set by the competition between parallel and cross-field transport in a first approximation. In the reported work, RFX-mod has operated in single-null configuration with X-point at the top wall. It follows that the parallel dissipation happens along the field line up to the strike region. Besides, it has been shown in Fig. 18 that the field lines intercept the wall at outboard midplane, opening a new channel for

parallel dissipation (limiter like). The importance of this relies on the fact that the transition to the outer layer, where limiter shadow becomes dominant, occurs in a range where the cross-field transport dominated by filaments is still relevant. Therefore, the plasma-wall interaction at outboard midplane is likely due to the combined contribution of parallel and cross-field transport. At the same time, the upper wall is dominated mainly by parallel transport in a divertor configuration, since cross-field turbulent transport in tokamak exhibits typically a ballooning character [54]. Note that this differs from standard tokamak configurations [78, 4], where the plasma-wall gap at the outboard midplane is larger.

The Integrated System of Internal Sensors (ISIS) is composed of a set of electrostatic and magnetic sensors, toroidally and poloidally arranged, installed on the wall of the RFX-mod [46]. In the present experiment, we considered only the poloidal electrostatic array, shown in Fig. 1, composed of 7 tungsten probes with 2 mm of diameter. Fig. 20 shows the measurements of the ISIS poloidal array during the L-H transition. The top panel shows the  $D_\alpha$  line signal as a reference for the L-H transition. The bottom part of Fig. 20 shows, respectively, the  $\phi_f$  moving averaged and its standard deviation ( $\sigma\phi_f$ ) over time, both calculated in 4 ms time slices. One can note that the ISIS poloidal array does not allow to perceive the strike point at the top, possibly due to the lack of poloidal resolution (Fig. 1 c). However, the outboard midplane shows a higher plasma-wall interaction, detected by both the mean and standard deviation of  $\phi_f$  (Fig. 20); the latter suggests that the transport into this point is composed by fluctuating processes. Indeed, the equilibrium reconstruction indicates that the magnetic field lines in the far SOL intercept the wall in this region, depicted by a relatively shorter connection length (Fig. 18). As observed in Fig. 19, blobs at the midplane far SOL are likely connected to the nearest wall. In addition, owing to the plasma-wall proximity, turbulent cross-field transport might also contribute to the plasma-wall interaction in this region. Since the LCFS-wall distance is  $< 3$  cm at the midplane and considering that the filaments radial velocity in the SOL during L-mode is  $\sim 2.0$  km/s, it follows that a blob would reach the wall in  $\tau_\perp < 15 \mu\text{s}$  coming from the near edge. Hence, fluctuations observed in ISIS at  $\theta \sim -15^\circ$  during L-mode are possibly the combination of parallel and cross-field transport. For sake of comparison, the parallel dissipation characteristic time, considering  $c_s \approx 27$  km/s and  $L_\parallel = 10 - 30$  m, is  $\tau_\parallel \approx L_\parallel/c_s \approx 0.3 - 1.0$  ms - a remarkable difference. Of course, different types of dissipation mechanisms, e.g., viscosity, ion-neutral collision, sheared flows, can act to damp the blob and reduce its cross-field velocity.

During H-mode, the mean floating potential and its fluctuation measured at  $\theta \sim -15^\circ$  significantly drop. This effect might be due to the contribution of both parallel and cross-field transport. It has been shown that blobs are strongly modified during biasing, notably, their cross-field velocity reduces to almost zero in the SOL (Fig. 13), suggesting that they become trapped in this region. The shorter effective radial correlation length in the SOL agrees with that (Fig. 6). On the other hand, blobs near the separatrix seem to scale according to the inertial regime (Fig. 15),

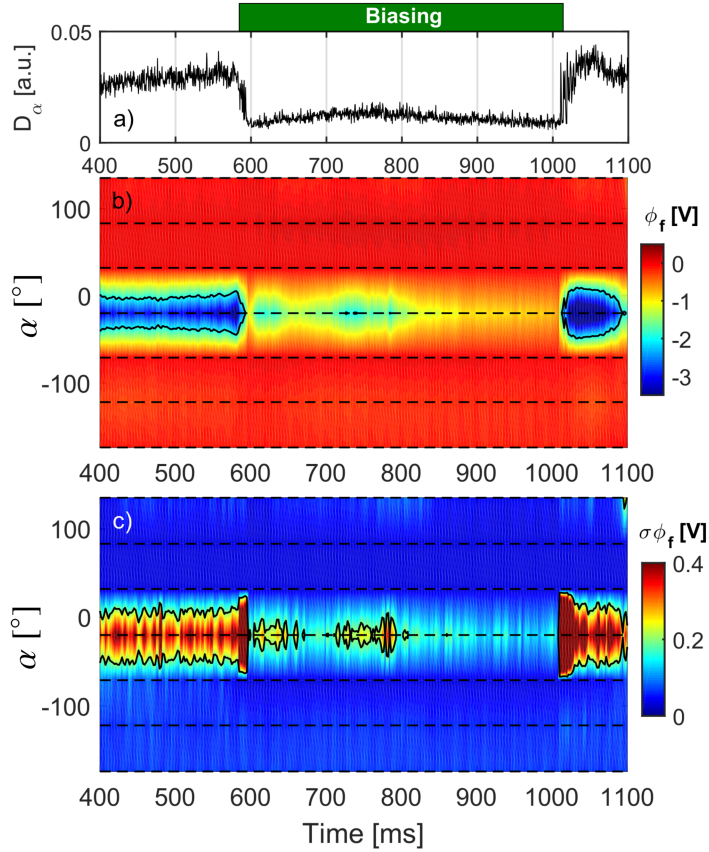


**Figure 20.** Plasma-wall interaction during the L-H transition measured with the ISIS poloidally array: a)  $D_\alpha$  line, b) mean floating potential ( $\phi_f$ ) with c) its standard deviation ( $\sigma\phi_f$ ) over time (calculated in 4 ms time slices); discharge #39136. The angle  $\alpha$  represents the poloidal position of the ISIS sensors (counterclockwise with respect to the midplane) as defined in Fig. 1 c).

suggesting that the parallel loss channel becomes negligible. The parallel current density represented in a 2D map seems to corroborate with that (Fig. 17, bottom). Therefore, both effects might contribute to the observed reduction of  $\phi_f$  and  $\sigma\phi_f$ , as seen in Fig. 20. However, one might argue that the trapping effect observed during biasing is the dominant factor because the blob velocity and amplitude sharply decrease in farther regions towards the wall. Such a result, in turn, affects the parallel dissipation indirectly since for a filament to contribute to the parallel dissipation at that point, it must reach the limiter shadow zone.

#### 4. Conclusions

In this paper, we report experimental observations of the blob dynamics in two scenarios in the RFX-mod operating as tokamak: ohmic L-mode and biasing induced ELM-free H-mode [41]. In both cases, floating potential coherent structures related to ion saturation current bursts through conditional average were successfully detected, tracked, and

characterized. The blobs were defined as the extreme events from the ion saturation current larger than  $2.5\sigma$ ; as also used in previous blob studies, e.g. [53, 4]. We observed (not shown here) that the threshold,  $2.5\sigma$ ,  $3.0\sigma$ , and  $3.5\sigma$ , does not change the blob dynamics and shape appreciably. However, a more systematic study of the impact of the threshold on the inferred blob shape and velocity will be left for future investigation. The 2D dynamic pattern recognizing based on the combination of cross-correlation and eigenvalue decomposition of the covariance matrix was applied in each time frame to depict the blob velocity and shape. In L-mode, a dipolar potential structure emerges near the plasma edge and propagates towards the SOL with its negative pole better depicted. For that reason, this part of the potential structure was taken as reference for the filament cross-field shape and velocity.

In L-mode, blobs were mainly aligned and stretched poloidally near the LCFS, while in the SOL, they become more circular and less tilted. Fast radial ejection from the edge was observed: the blob radial velocity increases as the potential structure approach the LCFS, decreasing in the SOL to values around  $\sim 2$  km/s. The blob amplitude and vorticity also increase in this process, slightly reducing later in the far SOL. The blob poloidal rotation was observed to be in the electron diamagnetic direction in the near edge, the same direction of the  $E \times B$  background poloidal projection velocity.

In H-mode, blobs were tracked from the SOL since they were more distinguishable within the observation frame in this region. The potential, in this case, seemed to be rather a negative monopole than a dipole. Near the LCFS, the potential blob is further stretched along the poloidal direction, reaching the highest radial velocity ( $\sim 4$  km/s). The poloidal rotation is in the ion diamagnetic direction in this region. Further out, the structure becomes trapped while its amplitude is gradually reduced. Such an effect was investigated through the comparison of the inverse of the blob characteristic time ( $1/\tau^{turb} = v_r L_\theta / L_r^2$ ) to the local  $E \times B$  shearing rate ( $\gamma_{E \times B} = B^{-1} dE_r / dr \approx B^{-1} d^2 \phi_f / dr^2$ ). According to [27], streamers or blobs are broken when  $\gamma_{E \times B} > 1/\tau^{turb}$ , analogous to the well known eddy decorrelation criterion [26]. While in L-mode,  $1/\tau^{turb}$  is always higher than  $\gamma_{E \times B}$ , in H-mode,  $\gamma_{E \times B}$  increases above L-mode values, satisfying, thus, the decorrelation criterion. We also pointed out that the vortex selection mechanism [63] by background sheared flows can yield the trapping effect observed in H-mode. Through this mechanism, a dipole can turn into a monopole, which would make the blob to spin rather than radially propagate [60]. Therefore, we conclude that the potential structure can be either suppressed directly, by means of the sheared flows [27], or indirectly by vortex selection; in this latter case, parallel losses can lead to its dissipation. Besides, since filaments are likely related to turbulence spreading in the plasma boundary, destabilizing flatter gradient regions in the far SOL, the findings reported here suggest a similar turbulence edge-SOL decoupling as observed in [12].

In addition, blobs dynamics in the two scenarios are discussed in the framework of analytical models and velocity scaling [6, 11]. In the sheath connected regime, blobs are typically electrically connected to a sheath along the field lines, where parallel dissipation

is responsible for the potential depletion. On the other hand, in the so-called inertial regime, blobs become disconnected, with the ion polarization current largely overcoming the parallel one. In L-mode, filaments can carry a current of approximately 20 mA with a large fraction flowing towards the sheath. The parallel current density and potential structure are roughly synchronized in this regime (Fig. 17, top). Blobs in L-mode were better described by the sheath connected scaling. However, due to the strong variation of the parallel connection length over the radial range covered by the probe, we observed a bifurcation in the velocity scaling. While near the LCFS, filaments are better described by the sheath connected at  $L_{\parallel} \approx 30$  m, in the far SOL, the better match happens at  $L_{\parallel} \approx 10$  m, roughly in accordance with the predicted  $L_{\parallel}$  in this region. In H-mode, however, filaments near the LCFS scale roughly according to the inertial regime. This study was aimed to investigate if the predictions of the analytical velocity scalings hold along the most likely blob trajectory from the conditional averaging. The results suggest that those predictions are sensitive to variations of background parameters, e.g., the ambient parallel connection length. We note that such a study can also be carried out by evaluating the dispersion of blob velocity and size by looking at single filaments. Although filaments can carry more current in H-mode, the larger electrical resistivity along the field lines suggests that perpendicular current closure might become important in this regime. We note that electromagnetic effects are likely negligible in this experiment. Nevertheless, it is worth noting that when plasma  $\beta$  is higher in the confinement region (e.g., during H-mode), electromagnetic features can be expected for large structures [76]. Lastly, we would like to emphasize that the strong effect of biasing on the blobs dynamics deeply affects the SOL properties. The reduction of the radial turbulence correlation length (Fig. 5) as well as the  $I_s$  e-folding length, and the plasma-wall interaction (Fig. 18) are examples of that. We believe that the results present in this paper contribute to a better understanding of cross-field transport in magnetized plasmas and the role of  $E \times B$  shear flows in regulating it.

## 5. Acknowledgements

This work has been carried out within the framework of the EUROfusion Consortium and has received funding from the Euratom research and training programme 2014-2018 and 2019-2020 under grant agreement No 633053 and from Erasmus Mundus International Doctoral College in Fusion Science and Engineering (FUSION-DC). The views and opinions expressed herein do not necessarily reflect those of the European Commission.

## References

- [1] J. A. Boedo, D. Rudakov, R. Moyer, S. Krasheninnikov, D. Whyte, G. McKee, G. Tynan, M. Schaffer, P. Stangeby, P. West, S. Allen, T. Evans, R. Fonck, E. Hollmann, A. Leonard, A. Mahdavi, G. Porter, M. Tillack, and G. Antar. Transport by intermittent convection in the boundary of the DIII-D tokamak. *Phys. Plasmas*, 8(11):4826–4833, 2001.

- [2] D. Carralero, S. Artene, M. Bernert, G. Birkenmeier, M. Faitsch, P. Manz, P. de Marne, U. Stroth, M. Wischmeier, E. Wolfrum, and and. On the role of filaments in perpendicular heat transport at the scrape-off layer. *Nucl. Fusion*, 58(9):096015, jul 2018.
- [3] S.J. Zweben, J.R. Myra, W.M. Davis, D.A. D’Ippolito, T.K. Gray, S.M. Kaye, B.P. LeBlanc, R.J. Maqueda, D.A. Russell, and D.P. Stotler and. Blob structure and motion in the edge and SOL of NSTX. *Plasma Phys. Control. Fusion*, 58(4):044007, 2016.
- [4] C. K. Tsui, J. A. Boedo, J. R. Myra, B. Duval, B. Labit, C. Theiler, N. Vianello, W. A. J. Vijvers, H. Reimerdes, S. Coda, O. Février, J. R. Harrison, J. Horacek, B. Lipschultz, R. Maurizio, F. Nespoli, U. Sheikh, K. Verhaegh, and N. Walkden. Filamentary velocity scaling validation in the TCV tokamak. *Phys. Plasmas*, 25(7):072506, 2018.
- [5] N. Vianello, D. Carralero, C.K. Tsui, V. Naulin, M. Agostini, I. Cziegler, B. Labit, C. Theiler, E. Wolfrum, D. Aguiam, S. Allan, M. Bernert, J. Boedo, S. Costea, H. De Oliveira, O. Fevrier, J. Galdon-Quiroga, G. Grenfell, A. Hakola, C. Ionita, H. Isliker, A. Karpushov, J. Kovacic, B. Lipschultz, R. Maurizio, K. McClements, F. Militello, A.H. Nielsen, J. Olsen, J.J. Rasmussen, T. Ravensbergen, H. Reimerdes, B. Schneider, R. Schrittwieser, E. Selunin, M. Spolaore, K. Verhaegh, J. Vicente, N. Walkden, W. Zhang, the ASDEX Upgrade Team, the TCV Team, and the EUROfusion MST1 Team. Scrape-off layer transport and filament characteristics in high-density tokamak regimes. *Nucl. Fusion*, 60(1):016001, 2019.
- [6] S.I. Krasheninnikov, D.A. D’ippolito, and J.R. Myra. Recent theoretical progress in understanding coherent structures in edge and SOL turbulence. *J. of Plasma Phys.*, 74(5):679–717, 2008.
- [7] D.A. D’Ippolito, J.R. Myra, and S.J. Zweben. Convective transport by intermittent blob-filaments: Comparison of theory and experiment. *Phys. Plasmas*, 18(6):060501, 2011.
- [8] G.Q. Yu and S.I. Krasheninnikov. Dynamics of blobs in scrape-off-layer/shadow regions of tokamaks and linear devices. *Phys. Plasmas*, 10(11):4413–4418, 2003.
- [9] S I Krasheninnikov. On scrape off layer plasma transport. *Physics Letters A*, 283(5-6):368–370, 2001.
- [10] O.E. Garcia, N.H. Bian, and W. Fundamenski. Radial interchange motions of plasma filaments. *Phys. Plasmas*, 13(8):082309, 2006.
- [11] J.R. Myra, D.A. Russell, and D.A. D’Ippolito. Collisionality and magnetic geometry effects on tokamak edge turbulent transport. I. A two-region model with application to blobs. *Phys. Plasmas*, 13(11):112502, 2006.
- [12] G.G. Grenfell, B.Ph. Van Milligen, U. Losada, W. Ting, B. Liu, C. Silva, M. Spolaore, and C. Hidalgo. Measurement and control of turbulence spreading in the Scrape-Off Layer of TJ-II. *Nucl. Fusion*, 59(1):016018, 2018.
- [13] T. Eich, A.W. Leonard, R.A. Pitts, W. Fundamenski, R.J. Goldston, T.K. Gray, A. Herrmann, A. Kirk, A. Kallenbach, O. Kardaun, A.S. Kukushkin, B. LaBombard, R. Maingi, M.A. Makowski, A. Scarabosio, B. Sieglin, J. Terry, A. Thornton, and and. Scaling of the tokamak near the scrape-off layer H-mode power width and implications for ITER. *Nucl. fusion*, 53(9):093031, 2013.
- [14] D.L Rudakov, J.A Boedo, R.A Moyer, P.C Stangeby, J.G Watkins, D.G Whyte, L Zeng, N.H Brooks, R.P Doerner, T.E Evans, M.E Fenstermacher, M Groth, E.M Hollmann, S.I Krasheninnikov, C.J Lasnier, A.W Leonard, M.A Mahdavi, G.R McKee, A.G McLean, A.Yu Pigarov, W.R Wampler, G Wang, W.P West, and C.P.C Wong. Far SOL transport and main wall plasma interaction in DIII-d. *Nucl. Fusion*, 45(12):1589–1599, nov 2005.
- [15] P. C. Stangeby. *The plasma boundary of magnetic fusion devices*. CRC Press, 2000.
- [16] J.R. Myra, D.A. Russell, D.A. D’Ippolito, J-W. Ahn, R. Maingi, R.J. Maqueda, D.P. Lundberg, D.P. Stotler, S.J. Zweben, and M.Umansky. Turbulent transport and the scrape-off-layer width. *J. Nucl. Mat.*, 415(1):S605, 2011.
- [17] C.S. Chang, S. Ku, A. Loarte, V. Parail, F. Köchl, M. Romanelli, R. Maingi, J.-W. Ahn, T. Gray, J. Hughes, B. LaBombard, T. Leonard, M. Makowski, and J. Terry. Gyrokinetic projection of the divertor heat-flux width from present tokamaks to iter. *Nucl. Fusion*, 57(11):116023, 2017.

- [18] O.E. Garcia, R. Kube, A. Theodorsen, and H.L. Pécseli. Stochastic modelling of intermittent fluctuations in the scrape-off layer: Correlations, distributions, level crossings, and moment estimation. *Phys. Plasmas*, 23(5):052308, 2016.
- [19] F. Militello and J.T. Omotani. Scrape off layer profiles interpreted with filament dynamics. *Nucl. Fusion*, 56(10):104004, 2016.
- [20] Ze-Yu Li, XQ Xu, Na-Mi Li, VS Chan, and Xiao-Gang Wang. Prediction of divertor heat flux width for ITER using BOUT++ transport and turbulence module. *Nucl. Fusion*, 59(4):046014, 2019.
- [21] P.H. Diamond, S.I. Itoh, K. Itoh, and T.S. Hahm. Zonal flows in plasma - a review. *Plasma Physics and Controlled Fusion*, 47(5):R35, 2005.
- [22] C. Hidalgo, M. A. Pedrosa, L. García, and A. Ware. Experimental evidence of coupling between sheared-flow development and an increase in the level of turbulence in the TJ-II stellarator. *Phys. Rev. E*, 70:067402, Dec 2004.
- [23] G. Grenfell, B. Ph. van Milligen, U. Losada, T. Estrada, B. Liu, C. Silva, M. Spolaore, C. Hidalgo, and TJ-II team. The impact of edge radial electric fields on edge-scrape-off layer coupling in the TJ-II stellarator. *Nucl. Fusion*, 60(1):014001, 2019.
- [24] A. Diallo, A. Fasoli, I. Furno, B. Labit, M. Podesta, and C. Theiler. Dynamics of plasma blobs in a shear flow. *Phys. Rev. Lett.*, 101(11):115005, 2008.
- [25] J.R. Myra, W.M. Davis, D.A. D’Ippolito, B. LaBombard, D.A. Russell, J.L. Terry, and S.J. Zweben. Edge sheared flows and the dynamics of blob-filaments. *Nucl. Fusion*, 53(7):073013, 2013.
- [26] K.H. Burrell. Effects of  $E \times B$  velocity shear and magnetic shear on turbulence and transport in magnetic confinement devices. *Phys. Plasmas*, 4(5):1499–1518, 1997.
- [27] N. Bisai, A. Das, S. Deshpande, R. Jha, P. Kaw, A. Sen, and R. Singh. Edge and scrape-off layer tokamak plasma turbulence simulation using two-field fluid model. *Phys. Plasmas*, 12(7):072520, 2005.
- [28] P. Ricci, B.N. Rogers, and S. Brunner. High-and low-confinement modes in simple magnetized toroidal plasmas. *Phys. Rev. Lett.*, 100(22):225002, 2008.
- [29] Ph. Ghendrih, G. Ciraolo, Y. Larmande, Y. Sarazin, P. Tamain, P. Beyer, G. Chiavassa, G. Darmet, X. Garbet, and V. Grandgirard. Shearing effects on density burst propagation in SOL plasmas. *J. Nucl. Mater.*, 390:425–427, 2009.
- [30] F. Wagner. A quarter-century of H-mode studies. *Plasma Phys. Control. Fusion*, 49(12 B):B1, 2007.
- [31] F. Ryter, L. Barrera Orte, B. Kurzan, R.M. McDermott, G. Tardini, E. Viezzer, M. Bernert, and R. Fischer and. Experimental evidence for the key role of the ion heat channel in the physics of the L-H transition. *Nucl. Fusion*, 54(8):083003, 2014.
- [32] J.J. Rasmussen, A.H. Nielsen, J. Madsen, V. Naulin, and G.S. Xu. Numerical modeling of the transition from low to high confinement in magnetically confined plasma. *Plasma Phys. Control. Fusion*, 58(1):014031, 2015.
- [33] E. J. Kim and P. H. Diamond. Zonal Flows and Transient Dynamics of the L-H Transition. *Phys. Rev. Lett.*, 90(18):185006, may 2003.
- [34] T. Windisch, O. Grulke, V. Naulin, and T. Klinger. Formation of turbulent structures and the link to fluctuation driven sheared flows. *Plasma Phys. Control. Fusion*, 53(12):124036, 2011.
- [35] N. Fedorczak, J.P. Gunn, J-Y. Pascal, Ph. Ghendrih, G. Van Oost, P. Monier-Garbet, and G.R. Tynan. Electrostatic transport in L-mode scrape-off layer plasmas of Tore Supra tokamak. II. Transport by fluctuations. *Phys. Plasmas*, 19(7):072314, 2012.
- [36] N. Fedorczak, P. Manz, S. Chakraborty Thakur, M. Xu, and G.R. Tynan. Zonal flow shear amplification by depletion of anisotropic potential eddies in a magnetized plasma: idealized models and laboratory experiment. *Plasma Phys. Control. Fusion*, 55(2):025011, 2013.
- [37] R. J. Taylor, M. L. Brown, B. D. Fried, H. Grote, J. R. Liberati, G. J. Morales, P. Pribyl, D. Darrow, and M. Ono. H-mode behavior induced by cross-field currents in a tokamak. *Phys.*

- Rev. Lett.*, 63(21):2365–2368, 1989.
- [38] J. Boedo, D. Gray, S. Jachmich, R. Conn, G.P. Terry, G. Tynan, G. Van Oost, R.R. Weynants, Textor Team, et al. Enhanced particle confinement and turbulence reduction due to  $E \times B$  shear in the TEXTOR tokamak. *Nucl. Fusion*, 40(7):1397, 2000.
- [39] G.G. Grenfell, I.C. Nascimento, D.S. Oliveira, Z.O. Guimarães-Filho, J. . Elizondo, A.P. Reis, R.M.O. Galvão, W.A.H. Baquero, A.M. Oliveira, G. Ronchi, W.P. de Sá, and J.H.F. Severo. H-mode access and the role of spectral shift with electrode biasing in the TCABR tokamak. *Phys. Plasmas*, 25(7):072301, 2018.
- [40] C. Hidalgo, M.A. Pedrosa, N. Dreval, K.J. McCarthy, L. Eliseev, M.A. Ochando, T. Estrada, I. Pastor, E. Ascasíbar, E. Calderón, A. Cappa, A.A. Chmyga, A. Fernández, B. Gonçalves, J. Hernanz, J.A. Jiménez, S.M. Khrebtov, A.D. Komarov, A.S. Kozachok, L. Krupnik, A. López-Fraguas, A. López-Sánchez, A.V. Melnikov, F. Medina, B. van Milligen, C. Silva, F. Tabarés, and D. Tafalla. Improved confinement regimes induced by limiter biasing in the TJ-II stellarator. *Plasma Phys. Control. Fusion*, 46(1):287, 2003.
- [41] M. Spolaore, R. Cavazzana, L. Marrelli, L. Carraro, P. Franz, S. Spagnolo, B. Zaniol, M. Zuin, L. Cordaro, S. Dal Bello, G. De Masi, A. Ferro, C. Finotti, L. Grando, G. Grenfell, P. Innocente, O. Kudlacek, G. Marchiori, E. Martines, B. Momo, R. Paccagnella, P. Piovesan, C. Piron, M.E. Puiatti, M. Recchia, P. Scarin, C. Taliercio, N. Vianello, and L. Zanotto. H-mode achievement and edge features in rfx-mod tokamak operation. *Nucl. Fusion*, 57(11):116039, 2017.
- [42] P. Sonato, G. Chitarin, P. Zaccaria, F. Gnesotto, S. Ortolani, A. Buffa, M. Bagatin, W.R. Baker, S. Dal Bello, P. Fiorentin, L. Grando, G. Marchiori, D. Marcuzzi, A. Masiello, S. Peruzzo, N. Pomaro, and G. Serianni. Machine modification for active MHD control in RFX. *Fusion engineering and design*, 66:161–168, 2003.
- [43] P. Zanca, L. Marrelli, G. Manduchi, and G. Marchiori. Beyond the intelligent shell concept: the clean-mode-control. *Nucl. Fusion*, 47(11):1425, 2007.
- [44] R. Paccagnella, S. Ortolani, P. Zanca, A. Alfieri, T. Bolzonella, L. Marrelli, M. E. Puiatti, G. Serianni, D. Terranova, M. Valisa, M. Agostini, L. Apolloni, F. Auriemma, F. Bonomo, A. Canton, L. Carraro, R. Cavazzana, M. Cavinato, P. Franz, E. Gazza, L. Grando, P. Innocente, R. Lorenzini, A. Luchetta, G. Manduchi, G. Marchiori, S. Martini, R. Pasqualotto, P. Piovesan, N. Pomaro, P. Scarin, G. Spizzo, M. Spolaore, C. Taliercio, N. Vianello, B. Zaniol, L. Zanotto, and M. Zuin. Active-feedback control of the magnetic boundary for magnetohydrodynamic stabilization of a fusion plasma. *Phys. Rev. Lett.*, 97(7):075001, 2006.
- [45] H.Y.W. Tsui, R.D. Bengtson, G.X. Li, H. Lin, M. Meier, Ch.P. Ritz, and A.J. Wootton. A new scheme for langmuir probe measurement of transport and electron temperature fluctuations. *Rev. Sci. Instrum.*, 63(10):4608–4610, 1992.
- [46] G. Serianni, W. Baker, and S. Dal Bello. High-spatial resolution edge electrostatic probe system for RFX. *Rev. Sci. Instrum.*, 74(3):1558–1562, 2003.
- [47] O. Kudlacek, P. Zanca, C. Finotti, G. Marchiori, R. Cavazzana, and L. Marrelli. Real time measurement of plasma macroscopic parameters on RFX-mod using a limited set of sensors. *Phys. Plasmas*, 22(10):102503, 2015.
- [48] M. Greenwald. Density limits in toroidal plasmas. *Plasma Phys. Control. Fusion*, 44(8):R27, 2002.
- [49] P. Sauter, T. Pütterich, F. Ryter, E. Viezzer, E. Wolfrum, G.D. Conway, R. Fischer, B. Kurzan, R.M. McDermott, and S.K. Rathgeber and. L-to H-mode transitions at low density in ASDEX Upgrade. *Nucl. Fusion*, 52(1):012001, 2011.
- [50] H. Kantz and T. Schreiber. *Nonlinear time series analysis*, volume 7. Cambridge university press, 2004.
- [51] F. Riva, N. Vianello, M. Spolaore, P. Ricci, R. Cavazzana, L. Marrelli, and S. Spagnolo. Three-dimensional simulations of plasma turbulence in the RFX-mod scrape-off layer and comparison with experimental measurements. *Physics of Plasmas*, 25(2):022305, 2018.
- [52] H. Johnsen, H.L. Pécseli, and J. Trulsen. Conditional eddies in plasma turbulence. *The Physics*

- of fluids*, 30(7):2239–2254, 1987.
- [53] D. Carralero, G. Birkenmeier, H.W. Müller, P. Manz, P. deMarne, S.H. Müller, F. Reimold, U. Stroth, M. Wischmeier, and E. Wolfrum and. An experimental investigation of the high density transition of the scrape-off layer transport in ASDEX upgrade. *Nuclear Fusion*, 54(12):123005, 2014.
  - [54] B. D. Scott. Drift wave versus interchange turbulence in tokamak geometry: Linear versus nonlinear mode structure. *Phys. Plasmas*, 12(6):062314, 2005.
  - [55] I Furno, C Theiler, D Lançon, A Fasoli, D Irají, P Ricci, M Spolaore, and N Vianello. Blob current structures in TORPEX plasmas: experimental measurements and numerical simulations. *Plasma Physics and Controlled Fusion*, 53(12):124016, 2011.
  - [56] T.A. Carter. Intermittent turbulence and turbulent structures in a linear magnetized plasma. *Phys. Plasmas*, 13(1):010701, 2006.
  - [57] L.N. Trefethen and D. Bau III. *Numerical linear algebra*, volume 50. Siam, 1997.
  - [58] J. Madsen, O. E. Garcia, J. Stærk Larsen, V. Naulin, A.H. Nielsen, and J.J. Rasmussen. The influence of finite larmor radius effects on the radial interchange motions of plasma filaments. *Phys. Plasmas*, 18(11):112504, 2011.
  - [59] G.S. Yun, W. Lee, M.J. Choi, J. Lee, H.K. Park, B. Tobias, C.W. Domier, N.C. Luhmann, A.J.H. Donné, and J.H. Lee. Two-dimensional visualization of growth and burst of the edge-localized filaments in kstar h-mode plasmas. *Phys. Rev. Lett.*, 107(4):045004, 2011.
  - [60] J.R. Myra, D.A. D’ippolito, S.I. Krasheninnikov, and G.Q. Yu. Convective transport in the scrape-off-layer by nonthermalized spinning blobs. *Phys. Plasmas*, 11(9):4267–4274, 2004.
  - [61] H. Biglari, P.H. Diamond, and P.W. Terry. Influence of sheared poloidal rotation on edge turbulence. *Phys. Fluids B: Plasma Phys.*, 2(1):1–4, 1990.
  - [62] N.R. Walkden, L. Easy, F. Militello, and J.T. Omotani. Dynamics of 3D isolated thermal filaments. *Plasma Phys. Control. Fusion*, 58(11):115010, 2016.
  - [63] P.S. Marcus, T. Kundu, and C. Lee. Vortex dynamics and zonal flows. *Phys. Plasmas*, 7(5):1630–1640, 2000.
  - [64] M. Spolaore, V. Antoni, R. Cavazzana, G. Regnoli, G. Serianni, E. Spada, N. Vianello, H. Bergsäter, and J.R. Drake. Effects of  $E \times B$  velocity shear on electrostatic structures. *Phys. Plasmas*, 9(10):4110–4113, 2002.
  - [65] M. Spolaore, V. Antoni, E. Spada, H. Bergsäter, R. Cavazzana, J.R. Drake, E. Martines, G. Regnoli, G. Serianni, and N. Vianello. Vortex-induced diffusivity in reversed field pinch plasmas. *Phys. Rev. Lett.*, 93(21):215003, 2004.
  - [66] R. Sanchez, D.E. Newman, J-N Leboeuf, and V.K. Decyk. Nature of turbulent transport across sheared zonal flows: insights from gyrokinetic simulations. *Plasma Phys. Control. Fusion*, 53(7):074018, 2011.
  - [67] V.H. Marques Rosas Fernandes, L.P.J. Kamp, G.J.F. Van Heijst, and H.J.H. Clercx. Interaction of monopoles, dipoles, and turbulence with a shear flow. *Phys. Fluids*, 28(9):093603, 2016.
  - [68] M. Spolaore, N. Vianello, M. Agostini, R. Cavazzana, E. Martines, P. Scarin, G. Serianni, E. Spada, M. Zuin, and V. Antoni. Direct measurement of current filament structures in a magnetic-confinement fusion device. *Phys. Rev. Lett.*, 102(16):165001, 2009.
  - [69] M. Spolaore, N. Vianello, I. Furno, D. Carralero, M. Agostini, J. A. Alonso, F. Avino, R. Cavazzana, G. De Masi, A. Fasoli, C. Hidalgo, E. Martines, B. Momo, A. Scaggion, P. Scarin, S. Spagnolo, G. Spizzo, C. Theiler, and M. Zuin. Electromagnetic turbulent structures: A ubiquitous feature of the edge region of toroidal plasma configurations. *Phys. Plasmas*, 22(1):012310, 2015.
  - [70] K. Kovařík, I. Duran, J. Stöckel, J. Seidl, J. Adamek, M. Spolaore, N. Vianello, P. Hacek, M. Hron, and R. Panek. Filamentary probe on the COMPASS tokamak. *Rev. Sci. Instrum.*, 88(3):035106, 2017.
  - [71] N. Vianello, V. Naulin, R. Schrittwieser, H. W. Müller, M. Zuin, C. Ionita, J. J. Rasmussen, F. Mehlmann, V. Rohde, R. Cavazzana, and M. Maraschek. Direct Observation of Current in

- Type-I Edge-Localized-Mode Filaments on the ASDEX Upgrade Tokamak. *Phys. Rev. Lett.*, 106:125002, Mar 2011.
- [72] M Spolaore, K Kovařík, J Stöckel, J Adamek, R Dejarnac, I Ďuran, M Komm, T Markovic, E Martines, R Panek, et al. Electromagnetic ELM and inter-ELM filaments detected in the COMPASS Scrape-Off Layer. *Nuclear Materials and Energy*, 12:844–851, 2017.
- [73] I. Furno, M. Spolaore, C. Theiler, N. Vianello, R. Cavazzana, and A. Fasoli. Direct two-dimensional measurements of the field-aligned current associated with plasma blobs. *Phys. Rev. Lett.*, 106(24):245001, 2011.
- [74] D.D. Ryutov and R.H. Cohen. Instability driven by sheath boundary conditions and limited to divertor legs. *Contributions to plasma physics*, 44(1-3):168–175, 2004.
- [75] C. Theiler, I. Furno, P. Ricci, A. Fasoli, B. Labit, S.H. Müller, and G. Plyushchev. Cross-field motion of plasma blobs in an open magnetic field line configuration. *Phys. Rev. Lett.*, 103(6):065001, 2009.
- [76] P. Manz, D. Carralero, G. Birkenmeier, H.W. Müller, S.H. Müller, G. Fuchert, B.D. Scott, and U. Stroth. Filament velocity scaling laws for warm ions. *Phys. Plasmas*, 20(10):102307, 2013.
- [77] P Manz, G Birkenmeier, D Carralero, G Fuchert, H W Müller, S H Müller, B D Scott, U Stroth, T T Ribeiro, and E Wolfrum. The influence of finite ion temperature on plasma blob dynamics. *Plasma Physics and Controlled Fusion*, 57(1):014012, 2014.
- [78] D. Carralero, P. Manz, L. Aho-Mantila, G. Birkenmeier, M. Brix, M. Groth, H. W. Müller, U. Stroth, N. Vianello, and E. Wolfrum. Experimental validation of a filament transport model in turbulent magnetized plasmas. *Phys. Rev. Lett.*, 115(21):215002, 2015.
- [79] J.A. Van Allen. Inference of magnetospheric currents from multipoint magnetic field measurements. *American journal of physics*, 74(9):809–814, 2006.
- [80] M Spolaore, N Vianello, M Agostini, R Cavazzana, E Martines, G Serianni, P Scarin, E Spada, M Zuin, and V Antoni. Magnetic and electrostatic structures measured in the edge region of the RFX-mod experiment. *Journal of Nuclear Materials*, 390:448–451, 2009.
- [81] P. Paruta, C. Beadle, P. Ricci, and C. Theiler. Blob velocity scaling in diverted tokamaks: A comparison between theory and simulation. *Phys. Plasmas*, 26(3):032302, 2019.
- [82] D. Abate and P. Bettini. An inverse equilibrium tool to define axisymmetric plasma equilibria. *Plasma Phys. Controll. Fusion*, 61(10):105016, 2019.
- [83] D. Abate, G. Marchiori, and F. Villone. Modelling and experimental validation of RFX-mod Tokamak shaped discharges. *Fusion Engineering and Design*, 2018.
- [84] I Predebon, B Momo, D Terranova, and P Innocente. MHD spectra and coordinate transformations in toroidal systems. *Phys. Plasmas*, 23(9):092508, 2016.
- [85] J.M. Finn and L. Chacón. Volume preserving integrators for solenoidal fields on a grid. *Phys. Plasmas*, 12(5):054503, 2005.